

DFT+U within the framework of linear combination of numerical atomic orbitals

Cite as: J. Chem. Phys. **156**, 234104 (2022); <https://doi.org/10.1063/5.0090122>

Submitted: 03 March 2022 • Accepted: 24 May 2022 • Accepted Manuscript Online: 26 May 2022 •

Published Online: 15 June 2022

Xin Qu, Peng Xu,  Hong Jiang, et al.



[View Online](#)



[Export Citation](#)



[CrossMark](#)

ARTICLES YOU MAY BE INTERESTED IN

[Density-functional theory vs density-functional fits](#)

The Journal of Chemical Physics **156**, 214101 (2022); <https://doi.org/10.1063/5.0091198>

[Cluster perturbation theory. VIII. First order properties for a coupled cluster state](#)

The Journal of Chemical Physics (2022); <https://doi.org/10.1063/5.0082585>

[Nature of chemical bond and potential barrier in an invariant energy-orbital picture](#)

The Journal of Chemical Physics **156**, 234102 (2022); <https://doi.org/10.1063/5.0088340>

[Learn More](#)

The Journal
of Chemical Physics **Special Topics** Open for Submissions

DFT+*U* within the framework of linear combination of numerical atomic orbitals

Cite as: J. Chem. Phys. 156, 234104 (2022); doi: 10.1063/5.0090122

Submitted: 3 March 2022 • Accepted: 24 May 2022 •

Published Online: 15 June 2022



View Online



Export Citation



CrossMark

Xin Qu,^{1,2} Peng Xu,¹ Hong Jiang,^{3,a)} Lixin He,^{2,b)} and Xinguo Ren^{4,5,c)}

AFFILIATIONS

¹ Rocket Force University of Engineering, Xi'an, 710025, Shaanxi, China

² CAS Key Laboratory of Quantum Information, University of Science and Technology of China, Hefei, 230026, Anhui, China

³ Beijing National Laboratory for Molecular Sciences, College of Chemistry and Molecular Engineering, Peking University, Beijing 100871, China

⁴ Institute of Physics, Chinese Academy of Sciences, Beijing 100190, China

⁵ Songshan Lake Materials Laboratory, Dongguan 523808, Guangdong, China

a) Electronic mail: jianghchem@pku.edu.cn

b) Electronic mail: helx@ustc.edu.cn

c) Author to whom correspondence should be addressed: renxg@iphy.ac.cn

ABSTRACT

We present a formulation and implementation of the density functional theory (DFT)+*U* method within the framework of linear combination of numerical atomic orbitals (NAO). Our implementation not only enables single-point total energy and electronic-structure calculations but also provides access to atomic forces and cell stresses, hence allowing for full structure relaxations of periodic systems. Furthermore, our implementation allows one to deal with non-collinear spin texture, with the spin-orbit coupling (SOC) effect treated self-consistently. The key aspect behind our implementation is a suitable definition of the correlated subspace when multiple atomic orbitals with the same angular momentum are used, and this is addressed via the “Mulliken charge projector” constructed in terms of the first (most localized) atomic orbital within the *d/f* angular momentum channel. The important Hubbard *U* and Hund *J* parameters can be estimated from a screened Coulomb potential of the Yukawa type, with the screening parameter either chosen semi-empirically or determined from the Thomas–Fermi screening model. Benchmark calculations are performed for four late transition metal monoxide bulk systems, i.e., MnO, FeO, CoO, and NiO, and for the 5*d*-electron compounds IrO₂. For the former type of systems, we check the performance of our DFT+*U* implementation for calculating bandgaps, magnetic moments, electronic band structures, as well as forces and stresses; for the latter, the efficacy of our DFT+*U*+SOC implementation is assessed. Systematic comparisons with available experimental results, especially with the results from other implementation schemes, are carried out, which demonstrate the validity of our NAO-based DFT+*U* formalism and implementation.

Published under an exclusive license by AIP Publishing. <https://doi.org/10.1063/5.0090122>

I. INTRODUCTION

The density functional theory (DFT) developed by Hohenberg, Kohn, and Sham^{1,2} uses the charge density as the basic variable to determine the ground state of interacting many-particle systems, which allows one to simulate systems of sizes that are prohibitively expensive for wave function based methods.³ Within DFT, suitable approximations can be designed to achieve excellent balance between accuracy and efficiency, and as such, DFT has been widely used for electronic structure calculations for a large variety of physical and chemical problems. However, within the popular local

(spin-) density approximation [L(S)DA] or generalized gradient approximations (GGAs), DFT encounters failures in several known situations—in particular, for strongly correlated materials, usually characterized by partially filled *d/f* electron states. These include transition metals (TM) and their oxides, rare-earth compounds, and lanthanides, to name a few, where L(S)DA/GGAs typically yield quantitatively or even qualitatively wrong results.

The failure of L(S)DA or GGAs in strongly correlated materials can be traced back to the large delocalization error,^{4–7} more often termed many-body self-interaction errors,⁸ and the static correlation error^{4,9,10} associated with these functionals. Many approaches have

been proposed to address these deficiencies, such as self-interaction corrected DFT,¹¹ hybrid functionals,^{12,13} the localized orbital scaling correction,^{5,7} fractional spin correction,⁶ and so on. Among these, the most popular approaches in solid-state physics are the combination of L(S)DA and GGAs with the non-perturbative many-body technique—dynamical mean-field theory (DMFT)^{14–19} and with a simpler mean-field-type correction based on the Hubbard model.^{20–22} The latter approach, commonly known as DFT+*U*,^{23–25} inherits the efficiency of L(S)DA/GGA but gains the strength of the Hubbard model in describing the physics of strongly correlated systems. Owing to its success in describing certain non-trivial properties arising from strong correlation, e.g., band-gap opening in transition metal oxides (TMO) and/or rare-earth compounds at a similar cost as L(S)DA/GGAs, DFT+*U* has become one of the most widely used first-principles approaches for strongly correlated (especially insulating) systems.

Being enormously successful in dealing with open-shell systems with partially filled *d/f* states, DFT+*U* has become a standard module available in many DFT code packages, based on various basis-set frameworks. For instance, it has been implemented within the full-potential all-electron linearized augmented plane-wave (LAPW) framework, as exemplified by the WIEN2k²⁵ and ELK²⁶ codes, and within the projector-augmented-wave (PAW) or norm-conserving pseudopotential based plane-wave framework, with Vienna *ab initio* simulation package (VASP),²⁷ Abinit,²⁸ and QUANTUM ESPRESSO^{29,30} as prominent examples. In recent years, the linear combination of numerical atomic orbitals (NAOs) has emerged as a versatile basis set framework for implementing both conventional local and semi-local density functional approximations (DFAs),^{31–36} hybrid functionals,^{37–40} and many-body perturbation theories.^{37,41,42} Compared to other basis set choices, NAOs are considered to be advantageous for simulating large-scale systems due to their compact size and strict locality in real space. Thus, the implementation of the DFT+*U* method within the NAO framework is of great interest. Similar to other numerical schemes, the key aspect for the DFT+*U* implementation is to define a suitable projector, which maps the full-orbital space where the first-principles DFT calculations are performed to a local, correlated subspace where the local orbitals behind the (generalized) Hubbard model are defined. The NAO-based DFT+*U* implementations have been reported for SIESTA,^{33,43} OpenMX,⁴⁴ and FHI-aims codes,⁴⁵ where the emphasis has been placed on the choice of the projector function, as well as their influence on the suitable *U* values and the obtained results. Experiences strongly suggest that the DFT+*U* cannot be taken as a black-box method, and a proper use of this approach requires a good understanding of the underlying technical aspects of a given implementation.

In this work, we report yet another implementation of the DFT+*U* method within ABACUS,³⁶ which is a first-principles code package based on the norm-conserving pseudopotentials and NAO basis functions. ABACUS allows one to use plane-wave basis functions as well, but our current DFT+*U* implementation is based on the NAO basis set framework and, hence, shares similarities with the OpenMX⁴⁴ and FHI-aims implementations.⁴⁵ However, due to the different strategies adopted for basis set generation, the resultant NAOs differ in shape and spatial extent, which further affects the projector and other implementation details. Our implementation not only supports usual self-consistent DFT+*U* electronic structure

calculations but also allows for force and stress computations, thus enabling full structural relaxations. Furthermore, non-collinear spin configurations and spin-orbit coupling (SOC) effects can be treated within our implementation, which is instrumental for systems containing heavy elements. Last but not least, we have made attempts to compute the Hubbard *U* value on the fly from a Yukawa-type screened Coulomb potential. The performance of such a scheme for determining the *U* value will be examined. Considering all these aspects, we believe that a concise description of the formulation and numerical details of our implementation should be not only useful for the users and developers of the ABACUS code but also of general interest to the electronic-structure community using the NAO basis sets.

This paper is organized as follows: In Sec. II, we present the detailed formulation behind our implementation, including the rotationally invariant DFT+*U* energy functional, our choice of the local projector, the force and stress evaluations, as well as the incorporation of SOC in the NAO-based DFT+*U* formalism and the determination of the *U*, *J* values from the Yukawa screened Coulomb potential. Section III presents the computational details in this paper. In Sec. IV, the efficacy of our formalism and the validity of our implementation will be examined. This is done by comparing the results of our implementation to those of experiments and particularly of other well-tested codes. Finally, we conclude this work in Sec. V.

II. FORMALISM

A. General DFT+*U* functional

The basic idea of DFT+*U* is to treat strongly correlated *d/f* electrons in terms of multi-orbital Hubbard model at the level of static Hartree–Fock mean-field theory, whereas all the rest electrons are described at the level of conventional density functional approximations (DFAs), such as L(S)DA and GGA. Since the *U* correction term in DFT+*U* corresponds to a Hartree–Fock approximation of the multi-orbital Hubbard model, the unphysical self-interactions among strongly correlated *d/f* electrons present in the Hartree energy are canceled out. This is considered as the main reason for the success of DFT+*U* in producing more reliable insulating gaps, magnetic moments, and other properties for TMOs.²⁵ The many-body complexity is encoded into the screened Coulomb interaction among strongly correlated *d/f* electrons, usually parameterized in terms of the Hubbard *U* for describing the direct Coulomb interaction and the Hund *J* for describing the exchange interaction.

The formulation of the DFT+*U* approach begins with the following energy functional:

$$E_{\text{DFT+}U} = E_{\text{DFA}} + E_U - E_{\text{dc}}, \quad (1)$$

where E_{DFA} is the energy of density functional approximations at the level of L(S)DA or GGA, and E_U is the Coulomb interaction energy due to strongly correlated electrons given by the Hartree–Fock approximation to the multi-orbital Hubbard model. The double counting term E_{dc} is subtracted here to discount the Coulomb interaction energy that is already included in DFAs at an average level.

Now we discuss the last two terms on the right-hand side of Eq. (1). Using the second-quantization language, the full electron-electron interaction term can be written as

$$\hat{H}_{\text{Hub}} = \frac{1}{2} \sum_{\{m\}} \sum_{\sigma\sigma'} \langle mm' | v_{\text{sc}} | m'' m''' \rangle \hat{c}_m^{\sigma\dagger} \hat{c}_{m'}^{\sigma'} \hat{c}_{m''}^{\sigma'} \hat{c}_{m'''}^{\sigma}, \quad (2)$$

where the Coulomb interaction matrix elements are

$$\begin{aligned} & \langle mm' | v_{\text{sc}} | m'' m''' \rangle \\ &= \int d\mathbf{r} \int d\mathbf{r}' \varphi_m^*(\mathbf{r}) \varphi_{m'}^*(\mathbf{r}') v_{\text{sc}}(\mathbf{r}, \mathbf{r}') \varphi_{m''}(\mathbf{r}) \varphi_{m'''}(\mathbf{r}'). \end{aligned} \quad (3)$$

In Eqs. (2) and (3), $v_{\text{sc}}(\mathbf{r}, \mathbf{r}')$ is the (statically) screened Coulomb potential, $\{m\}$ the local orbital indices for d or f subshell, σ the spin index and $\hat{c}_m^{\sigma\dagger}$, and \hat{c}_m^{σ} the creation and annihilation operators associated with the local correlated orbitals.

For simplicity, we neglect the spin-orbit coupling (SOC) effect at this stage. The generalized DFT+ U formalism that incorporates the SOC effect will be presented in Sec. II D. In this case, each Kohn-Sham (KS) spin orbital is a product of a spatial function $\psi_{n\mathbf{k}}(\mathbf{r})$ and a spin function. The ground state of the KS system is a Slater determinant formed by occupied KS spin-orbitals.⁴⁶ The Hartree-Fock approximation to the Hubbard Hamiltonian equation (2) can be obtained by evaluating its expectation value within the KS ground state $|0\rangle$, yielding the energy contribution as

$$\begin{aligned} E_U &= \langle 0 | \hat{H}_{\text{Hub}} | 0 \rangle \\ &= \frac{1}{2} \sum_{\{m\}, \sigma} \left\{ \left(\langle mm' | v_{\text{sc}} | m'' m''' \rangle \right. \right. \\ &\quad \left. \left. - \langle mm' | v_{\text{sc}} | m''' m'' \rangle \right) n_{m'' m}^{\sigma} n_{m''' m'}^{\sigma} \right. \\ &\quad \left. + \langle mm' | v_{\text{sc}} | m'' m''' \rangle n_{m'' m}^{\sigma} n_{m''' m'}^{-\sigma} \right\}. \end{aligned} \quad (4)$$

In Eq. (4), $n_{mm'}^{\sigma}$ is the local occupation matrix given by

$$\begin{aligned} n_{mm'}^{\sigma} &= \langle 0 | \hat{c}_{m'}^{\sigma\dagger} \hat{c}_m^{\sigma} | 0 \rangle \\ &= \frac{1}{N_{\mathbf{k}}} \sum_{n\mathbf{k}} f_{n\mathbf{k}}^{\sigma} \langle \psi_{n\mathbf{k}}^{\sigma} | m\sigma \rangle \langle m'\sigma | \psi_{n\mathbf{k}}^{\sigma} \rangle, \end{aligned} \quad (5)$$

with $f_{n\mathbf{k}}^{\sigma}$ being the occupation number of KS orbitals $|\psi_{n\mathbf{k}}^{\sigma}\rangle$. Here, $|\psi_{n\mathbf{k}}^{\sigma}\rangle = |\psi_{n\mathbf{k}}^{\sigma}\rangle |\sigma\rangle$ is a product of the spatial wavevector $|\psi_{n\mathbf{k}}^{\sigma}\rangle$, which is the Kohn-Sham wavefunction of the σ -spin component in the position space, and the spin function $|\sigma\rangle$. Similarly, the local spin orbital $|m\sigma\rangle = |\phi_m\rangle |\sigma\rangle$. Furthermore, $N_{\mathbf{k}}$ is the number of \mathbf{k} points in the Brillouin zone (BZ), which equals the number of unit cells in the Born-Von-Kármén (BvK) supercell under the periodic boundary condition. Equation (4) is the well-known rotationally invariant form of DFT+ U first proposed by Liechtenstein *et al.*⁴⁷ in 1995, whereby the local occupation number matrix $n_{mm'}^{\sigma}$ is the key quantity.

Since the local occupation matrix is symmetric, one can always introduce a unitary transformation to diagonalize it and arrives at

$$E_U = \frac{1}{2} U \sum_{mm', \sigma} \mathbf{n}_m^{\sigma} \mathbf{n}_{m'}^{-\sigma} + \frac{1}{2} (U - J) \sum_{m \neq m', \sigma} \mathbf{n}_m^{\sigma} \mathbf{n}_{m'}^{\sigma}. \quad (6)$$

Here, we use bold \mathbf{n} to denote the vector comprising the eigenvalues of the local occupation matrix. Furthermore, $U \equiv \langle mm' | v_{\text{sc}} | mm' \rangle$ and $J \equiv \langle mm' | v_{\text{sc}} | m'm' \rangle$ are the direct Coulomb and exchange integrals of the electrons in the correlated subspace, respectively, which are assumed to be isotropic, i.e., independent of the magnetic quantum number m . Note that the self-interaction is absent both in Eqs. (4) and (6). Theoretically, $\langle mm' | v_{\text{sc}} | mm' \rangle$ can be evaluated through Slater integrals, but the detailed form of the screened Coulomb interaction v_{sc} remains unknown, and therefore in practical calculations, U and J are most commonly treated as adjustable parameters or obtained via pragmatic schemes, such as constrained DFT,^{23,48–50} constrained random-phase approximation (RPA),^{51–54} or linear-response approach.³⁰

The double-counting term E_{dc} in Eq. (1) is an important portion of the DFT+ U theory and needs to be properly treated. Unfortunately, there are uncertainties for a rigorous definition of this term. This difficulty arises from the fact that local/semi-local DFAs are not orbital-resolved theories, and contributions from individual orbitals cannot be separated from one another. By now, there are two main double counting schemes used in practical DFT+ U calculations. One is the so-called “around mean field (AMF)” scheme and another is the “fully localized limit (FLL)” scheme.^{23,24,55} Both schemes are physically motivated. It is generally accepted that the former gives a better description of metallic systems while the latter one is more suitable for insulating systems.¹⁰ The FLL double counting term is given by

$$E_{\text{dc}} = \frac{1}{2} UN(N - 1) - \frac{1}{2} J \sum_{\sigma} N^{\sigma} (N^{\sigma} - 1), \quad (7)$$

where $N = \sum_{\sigma} N^{\sigma}$, and N^{σ} is the total number of correlated d or f electrons of spin σ . The FLL double counting term can be derived by assuming integer occupations of correlated d or f electrons in the atomic limit. In our implementation, the FLL scheme is used.

Subtracting the double counting term E_{dc} from E_U and making some simple derivation, the DFT+ U energy correction can be explicitly expressed as

$$\Delta E_{\text{DFT+}U} = E_U - E_{\text{dc}} = \frac{1}{2} (U - J) \sum_{m\sigma} (\mathbf{n}_m^{\sigma} - \mathbf{n}_{m'}^{\sigma} \mathbf{n}_m^{\sigma}). \quad (8)$$

Since the trace of an arbitrary matrix remains unchanged after the unitary transform, $\Delta E_{\text{DFT+}U}$ can also be rewritten as

$$\Delta E_{\text{DFT+}U} = \frac{1}{2} (U - J) \sum_{\sigma} \left[\sum_m n_{mm}^{\sigma} - \sum_{mm'} n_{mm'}^{\sigma} n_{m'm}^{\sigma} \right]. \quad (9)$$

The above energy correction functionals [Eqs. (8) and (9)] are the simplified form of the rotationally invariant scheme proposed by Dudarev *et al.*,⁵⁶ while still retaining the rotational invariance as the energy correction stays unchanged under unitary transformations of the given set of correlated orbitals. Within this functional, the DFT+ U total energy reduces to standard L(S)DA/GGA in the case of empty or full (0 or 1) occupation of local orbitals.

B. Mulliken charge projector

The DFT+ U formalism presented in Sec. II A only applies to the single-site case, i.e., only one correlated atom in the cell. To

deal with the multi-site cases, it is necessary to introduce an extra correlated atomic index I to label the local occupation matrix and the parameters U and J . Furthermore, in Sec. II A, it is implicitly assumed that the local correlated orbitals $\{|m\rangle\}$ are orthonormal to each other, and these are not necessarily satisfied for practically chosen local orbitals. Considering these complexities, it is convenient to introduce a local projection operator $P_{mm'}^\sigma$, called “projector,” such that the spin-dependent local occupation matrix is given by

$$n_{I,mm'}^\sigma = \frac{1}{N_k} \sum_{nk} f_{nk}^\sigma \langle \psi_{nk}^\sigma | \hat{P}_{I,mm'}^\sigma | \psi_{nk}^\sigma \rangle, \quad (10)$$

where I denotes a correlated atom to which the U correction needs to be applied. The key issue in the implementation of DFT+ U is to construct such a projector that maps the full Kohn–Sham orbital space into the correlated subspace. The choice of the projector depends on the underlying computational frameworks, ranging from the linear muffin-tin orbital method,²⁵ the LAPW method,²⁵ to the PAW method^{27,28} and pseudopotential-based plane-wave method.³⁰ Within the NAO-based framework, the most straightforward way is to utilize the local d/f -type atomic-orbital basis functions to construct the projector. However, in practical calculations, the NAOs centering on neighboring atoms have finite overlaps, i.e., they are non-orthogonal to each other. This non-orthogonality has to be taken into account when defining a suitable projector. In this regard, we follow the previous work of Han *et al.*⁴⁴ where the so-called “Mulliken charge projector” is used. This projector has the nice property that the sum rule is satisfied, in the sense that the total electronic charges are conserved when summing up partial charges over all projected channels.

Specifically, one needs to define dual orbitals associated with the original atomic orbitals as

$$\tilde{\phi}_{k\mu}(\mathbf{r}) = \sum_v \phi_{kv}(\mathbf{r}) S_{v\mu}^{-1}(\mathbf{k}), \quad (11)$$

where

$$\phi_{kv}(\mathbf{r}) = \sum_{\mathbf{R}} e^{i\mathbf{k}\mathbf{R}} \phi_v^{\mathbf{R}}(\mathbf{r}) \quad (12)$$

is the Bloch summation of NAOs. $\phi_v^{\mathbf{R}}(\mathbf{r}) = \phi_v(\mathbf{r} - \boldsymbol{\tau}_a - \mathbf{R})$ denotes a NAO centering on the a th atom within the unit cell \mathbf{R} . The orbital indices μ and v are a combination of $\{a, l, \zeta, m\}$, with a labeling the atomic site, l , m the angular and magnetic momentum, and ζ the multiplicity (different radial functions) for a given l , respectively. Furthermore, $S_{\mu\nu}(\mathbf{k})$ is the overlap matrix in reciprocal space³⁶

$$S_{\mu\nu}(\mathbf{k}) = \langle \phi_{k\mu} | \phi_{kv} \rangle = \sum_{\mathbf{R}} e^{-i\mathbf{k}\mathbf{R}} \langle \phi_{\mu}^{\mathbf{R}} | \phi_v^{\mathbf{R}} \rangle. \quad (13)$$

Here, we follow the convention that the extended Bloch orbitals are normalized within the BvK supercell cell and the real-space integration indicated by the braket goes over the supercell cell. It can be readily shown that the dual and original Bloch orbitals satisfy the following biorthogonality relation:

$$\langle \phi_{k\mu} | \tilde{\phi}_{kv} \rangle = \delta_{kq} \delta_{\mu\nu}. \quad (14)$$

Making use of the dual orbitals, we define the projector used in the present work as

$$\hat{P}_{I,mm'}^\sigma = \frac{1}{4N_k} \sum_{\mathbf{k}} \left(|\tilde{\phi}_{k,\beta m'}^\sigma \rangle \langle \phi_{k,\beta m}^\sigma| + |\phi_{k,\beta m'}^\sigma \rangle \langle \tilde{\phi}_{k,\beta m}^\sigma| + |\tilde{\phi}_{k,\beta m}^\sigma \rangle \langle \phi_{k,\beta m'}^\sigma| + |\phi_{k,\beta m}^\sigma \rangle \langle \tilde{\phi}_{k,\beta m'}^\sigma| \right), \quad (15)$$

where the index β groups together the indices $\{I, l, \zeta\}$ with l and ζ belonging to the correlated channel of the correlated atom I . Note that this projector is slightly different from that introduced in the work of Han *et al.*,⁴⁴ which is essentially an average of the first two terms in Eq. (15). The local occupation matrices yielded by the projector used in Ref. 44 are Hermitian but not necessarily real symmetric. For convenience and numerical simplicity, we symmetrize the projector as is done in Eq. (15), and then the resultant local occupation matrix is guaranteed to be real and symmetric. This is consistent with the feature that the “on-site” global KS density matrix is also real and symmetric. Inserting Eq. (15) into Eq. (10), we arrive at

$$n_{I,mm'}^\sigma = \frac{1}{4N_k} \sum_{\mathbf{k}} \sum_{\mu} \left(S_{\beta m, \mu}(\mathbf{k}) \rho_{\mu, \beta m'}^\sigma(\mathbf{k}) + \rho_{\beta m, \mu}^\sigma(\mathbf{k}) S_{\mu, \beta m'}(\mathbf{k}) \right. \\ \left. + S_{\beta m', \mu}(\mathbf{k}) \rho_{\mu, \beta m}^\sigma(\mathbf{k}) + \rho_{\beta m', \mu}^\sigma(\mathbf{k}) S_{\mu, \beta m}(\mathbf{k}) \right), \quad (16)$$

where $\rho_{\mu\nu}^\sigma(\mathbf{k})$ is the spin-dependent KS density matrix

$$\rho_{\mu\nu}^\sigma(\mathbf{k}) = \sum_n f_{nk}^\sigma c_{nk, \mu}^\sigma c_{nk, \nu}^{\sigma*} \quad (17)$$

with $c_{nk, \mu}^\sigma$ being the KS eigenvectors, satisfying the generalized orthogonality relationship

$$\sum_{\mu, \nu} c_{nk, \mu}^\sigma S_{\mu\nu}(\mathbf{k}) c_{n'k, \nu}^{\sigma*} = \delta_{nn'}. \quad (18)$$

If we project the KS density matrix to all local atomic orbital channels and sum the traces of the resultant local occupation matrices up, i.e., requiring that β, m go over all the basis indices $\{a, l, \zeta, m\}$, one then obtains

$$\sum_{\sigma, v} n_{vv}^\sigma = \frac{1}{4N_k} \sum_{\sigma} \sum_{\mathbf{k}} \sum_{\mu, \nu} \left(S_{v, \mu}(\mathbf{k}) \rho_{\mu, v}^\sigma(\mathbf{k}) + \rho_{v, \mu}^\sigma(\mathbf{k}) S_{\mu, v}(\mathbf{k}) \right. \\ \left. + S_{v, \mu}(\mathbf{k}) \rho_{\mu, v}^\sigma(\mathbf{k}) + \rho_{v, \mu}^\sigma(\mathbf{k}) S_{\mu, v}(\mathbf{k}) \right) \\ = \frac{1}{N_k} \sum_{n, \sigma} f_{nk}^\sigma = N_e, \quad (19)$$

where N_e is the total number of electrons in one unit cell. In deriving Eq. (19), the orthogonality relationship [Eq. (18)] is used. Equation (19) is the above-mentioned sum rule satisfied by the “Mulliken charge operator.”

C. Effective potential, force, and stress

To perform self-consistent DFT+ U calculations and enable structure relaxations, one needs to derive the expressions of the effective single-particle potential and the forces and stresses

corresponding to the DFT+ U energy functional. To this end, we first generalize the single-site DFT+ U energy correction as given by Eq. (9) to the multi-site case,

$$\Delta E_{\text{DFT}+U} = \frac{1}{2} \sum_I \bar{U}_I \sum_\sigma \{ \text{Tr}(n_I^\sigma) - \text{Tr}(n_I^\sigma n_I^\sigma) \}, \quad (20)$$

where $\bar{U}_I = U_I - J_I$ is the effective interaction parameter on the correlated atom I . Again, the isotropy of the interaction parameters is assumed. The contribution of the energy correction $\Delta E_{\text{DFT}+U}$ to the KS effective potential operator is given by its derivative with respect to the \mathbf{k} -dependent density matrix operator

$$\hat{\rho}_{\mathbf{k}}^\sigma = \frac{1}{N_{\mathbf{k}}} \sum_n f_{nk}^\sigma |\psi_{nk}^\sigma \sigma\rangle \langle \psi_{nk}^{\sigma,\dagger} \sigma|. \quad (21)$$

That is,

$$\begin{aligned} \Delta \hat{V}_{\text{eff}}^\sigma(\mathbf{k}) &= \frac{\delta \Delta E_{\text{DFT}+U}}{\delta \hat{\rho}_{\mathbf{k}}^\sigma} \\ &= \sum_I \sum_{mm'} \Delta V_{I,mm'}^\sigma \hat{P}_{I,mm'}^\sigma(\mathbf{k}), \end{aligned}$$

where

$$\Delta V_{I,mm'}^\sigma = \bar{U}_I (1/2 \delta_{mm'} - n_{I,mm'}^\sigma) \quad (22)$$

is the correction to the effective single-particle potential in the local subspace, and

$$\begin{aligned} \hat{P}_{I,mm'}^\sigma(\mathbf{k}) &= \frac{1}{4} (|\tilde{\phi}_{\mathbf{k},\beta m'} \sigma\rangle \langle \phi_{\mathbf{k},\beta m} \sigma| + |\phi_{\mathbf{k},\beta m'}^\sigma \rangle \langle \tilde{\phi}_{\mathbf{k},\beta m} \sigma| \\ &\quad + |\tilde{\phi}_{\mathbf{k},\beta m} \sigma\rangle \langle \phi_{\mathbf{k},\beta m'} \sigma| + |\phi_{\mathbf{k},\beta m}^\sigma \rangle \langle \tilde{\phi}_{\mathbf{k},\beta m'} \sigma|) \end{aligned} \quad (23)$$

is the \mathbf{k} -dependent Mulliken projector. The matrix form of the effective potential within the full NAO basis set is given by

$$\begin{aligned} \Delta V_{\text{eff},\mu\nu}^\sigma(\mathbf{k}) &= \langle \phi_{\mathbf{k}\mu} | \Delta \hat{V}_{\text{eff}}^\sigma(\mathbf{k}) | \phi_{\mathbf{k}\nu} \rangle \\ &= \sum_{\mathbf{R}} e^{-i\mathbf{k}\mathbf{R}} \langle \phi_{\mu}^\sigma(\mathbf{R}) | \Delta \hat{V}_{\text{eff}}^\sigma(\mathbf{k}) | \phi_{\nu}^\sigma(\mathbf{0}) \rangle \\ &= \frac{1}{4} \sum_I \sum_{mm'} \Delta V_{I,mm'}^\sigma \{ S_{\beta m,\nu}(\mathbf{k}) \delta_{\mu,\beta m'} \\ &\quad + S_{\mu,\beta m'}(\mathbf{k}) \delta_{\beta m,\nu} + S_{\beta m',\nu}(\mathbf{k}) \delta_{\mu,\beta m} + S_{\mu,\beta m}(\mathbf{k}) \delta_{\beta m',\nu} \}, \end{aligned} \quad (24)$$

which is to be added to DFA Hamiltonian matrix to obtain the DFT+ U one. As shown in Eq. (22), in the case of diagonal half-integer occupations, the DFT+ U Hamiltonian reduces to standard DFAs.

The contribution of the energy correction $\Delta E_{\text{DFT}+U}$ to the force on the a th atom can be evaluated by its derivative with respect to the atomic coordinate τ_a ,

$$F_a = \frac{d \Delta E_{\text{DFT}+U}}{d \tau_a} = \sum_\sigma \sum_I \sum_{mm'} \Delta V_{I,mm'}^\sigma \frac{dn_{I,mm'}^\sigma}{d\tau_a}, \quad (25)$$

which implies that the force due to the DFT+ U energy correction stems entirely from the change of the local occupation matrix in response to the atomic displacement. According to Eq. (16), the

change of the local occupation matrix can arise either from the change of the overlap matrix S or from that of the KS density matrix ρ , namely,

$$\frac{dn_{I,mm'}^\sigma[S, \rho]}{d\tau_a} = \frac{\partial n_{I,mm'}^\sigma[S, \rho]}{\partial S} \Bigg|_{\rho} \frac{\partial S}{\partial \tau_a} + \frac{\partial n_{I,mm'}^\sigma[S, \rho]}{\partial \rho} \Bigg|_S \frac{\partial \rho}{\partial \tau_a}. \quad (26)$$

Thus, the force correction brought by DFT+ U is also split into two contributions. The first contribution, arising from the change of the overlap matrix, is given by

$$\begin{aligned} &\sum_\sigma \sum_I \sum_{mm'} \Delta V_{I,mm'}^\sigma \frac{\partial n_{I,mm'}^\sigma[S, \rho]}{\partial S} \Bigg|_{\rho} \frac{\partial S}{\partial \tau_a} \\ &= \sum_\sigma \frac{1}{4N_{\mathbf{k}}} \sum_{\mathbf{k}} \sum_I \sum_{mm'} \Delta V_{I,mm'}^\sigma \sum_{\mu \in a} \\ &\quad \times \left(\frac{dS_{\beta m,\mu}(\mathbf{k})}{d\mathbf{r}_{\beta m,\mu}} \rho_{\mu,\beta m'}^\sigma(\mathbf{k}) + \rho_{\mu,\beta m}^{\sigma*}(\mathbf{k}) \frac{dS_{\beta m',\mu}^*(\mathbf{k})}{d\mathbf{r}_{\beta m',\mu}} \right. \\ &\quad \left. + \frac{dS_{\beta m',\mu}(\mathbf{k})}{d\mathbf{r}_{\beta m',\mu}} \rho_{\mu,\beta m}^\sigma(\mathbf{k}) + \rho_{\mu,\beta m'}^{\sigma*}(\mathbf{k}) \frac{dS_{\beta m,\mu}^*(\mathbf{k})}{d\mathbf{r}_{\beta m,\mu}} \right) \\ &\quad + \sum_\sigma \frac{1}{4N_{\mathbf{k}}} \sum_{\mathbf{k}} \sum_I \sum_{ammm'} \Delta V_{I,mm'}^\sigma \sum_\mu \\ &\quad \times \left(\frac{dS_{\mu,\beta m}^*(\mathbf{k})}{d\mathbf{r}_{\mu,\beta m}} \rho_{\beta m',\mu}^{\sigma*}(\mathbf{k}) + \rho_{\beta m,\mu}^{\sigma*}(\mathbf{k}) \frac{dS_{\mu,\beta m'}(\mathbf{k})}{d\mathbf{r}_{\mu,\beta m'}} \right. \\ &\quad \left. + \frac{dS_{\mu,\beta m'}^*(\mathbf{k})}{d\mathbf{r}_{\mu,\beta m'}} \rho_{\beta m,\mu}^{\sigma*}(\mathbf{k}) + \rho_{\beta m',\mu}^{\sigma*}(\mathbf{k}) \frac{dS_{\mu,\beta m}(\mathbf{k})}{d\mathbf{r}_{\mu,\beta m}} \right), \end{aligned} \quad (27)$$

where $\mathbf{r}_{v,\mu} = \tau_{a_\mu} - \tau_{a_v}$, with a_v and a_μ refer to the atoms that the NAO basis functions v and μ are centering on, respectively. In the above derivation, we have used the Hermiticity of the overlap and density matrix and the following relationship for the two-center integrals:

$$\frac{\partial \langle \phi_v | \phi_\mu \rangle}{\partial \tau_a} = \begin{cases} \left\langle \phi_v \left| \frac{\phi_\mu}{d\tau_a} \right. \right\rangle = \frac{d \langle \phi_v | \phi_\mu \rangle}{d\mathbf{r}_{v,\mu}}, & \mu \in a, v \notin a, \\ \left\langle \phi_\mu \left| \frac{d\phi_v}{d\tau_a} \right. \right\rangle = \frac{d \langle \phi_\mu | \phi_v \rangle}{d\mathbf{r}_{\mu,v}}, & \mu \notin a, v \in a, \\ 0, & \mu \in a, v \in a \text{ or } \mu \notin a, v \notin a. \end{cases} \quad (28)$$

The second part of the force consists in the contribution from the change of KS density matrix. Similarly, it is denoted as $\frac{\partial n_{I,mm'}^\sigma}{\partial \tau_a}|_S$, which means that overlap matrix is fixed. Its contribution to the total force is given by

$$\begin{aligned}
 & \sum_{\sigma} \sum_I \sum_{mm'} \Delta V_{I,mm'}^{\sigma} \frac{\partial n_{I,mm'}^{\sigma}[S, \rho]}{\partial \rho} \Big|_S \frac{\partial \rho}{\partial \tau_a} \\
 &= \sum_{\sigma} \frac{1}{4N_k} \sum_{\mathbf{k}} \sum_I \sum_{mm'} \Delta V_{I,mm'}^{\sigma} \sum_{\mu} \\
 & \quad \times \left(S_{\beta m, \mu}(\mathbf{k}) \frac{d\rho_{\mu, \beta m'}^{\sigma}(\mathbf{k})}{d\tau_a} + \frac{d\rho_{\beta m, \mu}^{\sigma}(\mathbf{k})}{d\tau_a} S_{\mu, \beta m'}(\mathbf{k}) \right. \\
 & \quad \left. + S_{\beta m', \mu}(\mathbf{k}) \frac{d\rho_{\mu, \beta m'}^{\sigma}(\mathbf{k})}{d\tau_a} + \frac{d\rho_{\beta m', \mu}^{\sigma}(\mathbf{k})}{d\tau_a} S_{\mu, \beta m}(\mathbf{k}) \right) \\
 &= \frac{1}{N_k} \sum_{\mathbf{k}} \sum_{\mu \nu} \Delta V_{\text{eff}, \nu \mu}^{\sigma}(\mathbf{k}) \frac{d\rho_{\mu \nu}^{\sigma}}{d\tau_a}(\mathbf{k}). \tag{29}
 \end{aligned}$$

This term is the so-called orthogonality force: $\sum_{\mu \nu} H_{\nu \mu} \partial \rho_{\mu \nu} / \partial \tau_a$. Readers who are interested in the detailed derivation of this term are referred to Refs. 33 and 36. However, this term requires no additional treatment here since it has already been properly included in orthogonality force term via the usual DFA calculation procedure.

The stress is defined as the derivative of the total energy with respect to the strain tensor. An efficient evaluation of the stress tensor is essential for relaxing the shape and size of the unit cell of periodic systems. The stress contribution from the DFT+U energy correction can be expressed as

$$\sigma_{\gamma \eta} = \frac{\partial \Delta E_{\text{DFT+U}}}{\partial \epsilon_{\gamma \eta}} = \sum_{\sigma} \sum_I \sum_{mm'} V_{I,mm'}^{\sigma} \frac{\partial n_{I,mm'}^{\sigma}}{\partial \epsilon_{\gamma \eta}}, \tag{30}$$

where γ and η denote the Cartesian coordinate indices and ϵ the strain tensor. As pointed out in Ref. 33, stress calculations require very little extra effort beyond multiplying the counterpart of the force by $\mathbf{r}_{\mu, \nu}^{\eta}$, where $\mathbf{r}_{\mu, \nu}$ is the vector connecting the atoms where the NAO basis functions ϕ_{μ} and ϕ_{ν} are centering on. Therefore, similar to the case of force calculations [cf. Eq. (26)], the contributions to the stress can also be decomposed into two parts. The first part $\frac{\partial n_{I,mm'}^{\sigma}}{\partial \epsilon_{\gamma \eta}}|_{\rho}$, arising from the derivative of the overlap matrix with respect to the strain tensor, is given by

$$\begin{aligned}
 \sum_{\sigma} \sum_I \sum_{mm'} V_{I,mm'}^{\sigma} \frac{\partial n_{I,mm'}^{\sigma}}{\partial \epsilon_{\gamma \eta}}|_{\rho} &= \sum_{\sigma} \frac{1}{4N_k} \sum_{\mathbf{k}} \sum_I \sum_{mm'} V_{I,mm'}^{\sigma} \sum_{\mu} \\
 & \quad \times \left(\rho_{\mu, \beta m'}^{\sigma}(\mathbf{k}) \sum_{\mathbf{R}} \frac{dS_{\beta m, \mu}(\mathbf{R})}{d\mathbf{r}_{\beta m, \mu}^{\gamma}} \mathbf{r}_{\beta m, \mu}^{\eta} e^{-i\mathbf{k}\mathbf{R}} \right. \\
 & \quad + \rho_{\beta m, \mu}^{\sigma}(\mathbf{k}) \sum_{\mathbf{R}} \frac{dS_{\mu, \beta m'}(\mathbf{R})}{d\mathbf{r}_{\mu, \beta m'}^{\gamma}} \mathbf{r}_{\mu, \beta m'}^{\eta} e^{-i\mathbf{k}\mathbf{R}} \\
 & \quad + \rho_{\mu, \beta m}^{\sigma}(\mathbf{k}) \sum_{\mathbf{R}} \frac{dS_{\beta m', \mu}(\mathbf{R})}{d\mathbf{r}_{\beta m', \mu}^{\gamma}} \mathbf{r}_{\beta m', \mu}^{\eta} e^{-i\mathbf{k}\mathbf{R}} \\
 & \quad \left. + \rho_{\beta m', \mu}^{\sigma}(\mathbf{k}) \sum_{\mathbf{R}} \frac{dS_{\mu, \beta m}(\mathbf{R})}{d\mathbf{r}_{\mu, \beta m}^{\gamma}} \mathbf{r}_{\mu, \beta m}^{\eta} e^{-i\mathbf{k}\mathbf{R}} \right). \tag{31}
 \end{aligned}$$

The second part of the stress is the counterpart of the orthogonality force term [cf. Eq. (29)]. For the same reason as in force calculations, this term has been included automatically in the total orthogonality stress in usual DFA calculations and requires no

additional treatment. Hence, for brevity, its explicit expression is not given here.

D. Spin-orbit coupling

In the discussion of the NAO-based DFT+U formalism presented earlier, the SOC effect is neglected. Physically, the SOC stems from the interaction between the intrinsic magnetic moment of the electrons and the magnetic field induced by their orbital angular momenta and is a consequence of the relativistic effect. The magnitude of the SOC increases with the atomic number; for systems containing heavy elements, such effect must be taken into account to obtain physically meaningful results. Below we discuss how SOC is incorporated in our DFT+U implementation.

When the SOC is present, the KS eigenstates $|\psi_{nk}\rangle$ become two-component spinors

$$|\psi_{nk}\rangle = \sum_{\mu} \begin{pmatrix} c_{n\mu, k}^{\uparrow} \\ c_{n\mu, k}^{\downarrow} \end{pmatrix} |\phi_{k\mu}\rangle = |\psi_{nk}^{\uparrow}\rangle | \uparrow \rangle + |\psi_{nk}^{\downarrow}\rangle | \downarrow \rangle, \tag{32}$$

where $| \uparrow \rangle$ and $| \downarrow \rangle$ are the up- and down-channel spin states, and $\psi_{nk}^{\uparrow}(\mathbf{r})$ and $\psi_{nk}^{\downarrow}(\mathbf{r})$ are the associated spatial wave functions. The two-component spinor can be regarded as a superposition state of its two components: state $|\Psi_{nk}^{\uparrow}\rangle$ multiplied with spin-up function and state $|\Psi_{nk}^{\downarrow}\rangle$ with spin-down function. The form of such two-component eigenstates is different from the one-component eigenstates $\Psi_{nk}^{\sigma}(\mathbf{r})$ of the non-SOC Hamiltonian, whereby the variables of spin σ and position \mathbf{r} are independent. In the spirit of the method of separation of variables, the eigenstates $\Psi_{nk}^{\sigma}(\mathbf{r})$ is product of a function of the position $\Psi_{nk}(\mathbf{r})$ and a eigenstate of spin variables $\alpha_n(\sigma)$ with eigenvalue σ . Obviously, the $|\Psi_{nk}\rangle$ in Eq. (32) cannot be reduced to such a form.

The DFT+U energy functional is given by the expectation value of the second-quantized Hubbard Hamiltonian, i.e., Eq. (2), in the local subspace within the Hartree-Fock ground-state, given by the Slater determinant that is formed by the lowest N spinors. After some simple derivations, we obtain

$$\begin{aligned}
 E_U &= \frac{1}{2} \sum_I \sum_{\{m\}} \sum_{\sigma \sigma'} \langle mm' | v_{sc} | m'' m''' \rangle n_{I,mm''}^{\sigma \sigma'} n_{I,m'm''}^{\sigma' \sigma'} \\
 &\quad - \frac{1}{2} \sum_I \sum_{\{m\}} \sum_{\sigma \sigma'} \langle mm' | v_{sc} | m''' m'' \rangle n_{I,mm''}^{\sigma \sigma'} n_{I,m'm''}^{\sigma' \sigma}. \tag{33}
 \end{aligned}$$

The $n_{I,mm'}^{\sigma \sigma'}$ is the local occupation matrix within the SOC scheme that will be addressed later. Following a similar procedure as Eqs. (4)–(6), one can also introduce a unitary transformation to Eq. (33) and then arrive at

$$E_U = \frac{1}{2} \sum_I U_I \sum_{mm'} \sum_{\sigma} \mathbf{n}_{I,\sigma m} \mathbf{n}_{I,-\sigma m'} + \frac{1}{2} \sum_I (U_I - J_I) \sum_{m \neq m'} \sum_{\sigma} \mathbf{n}_{I,\sigma m} \mathbf{n}_{I,\sigma m'}. \tag{34}$$

In this derivation, the $n_{I,mm'}^{\sigma \sigma'}$ is regarded as a local occupation matrix in the spin-orbit representation rather a four-order tensor, i.e., σm is a compact index of spin-orbit. The $\mathbf{n}_{I,\sigma m}$ is the diagonalized local occupation matrix of $n_{I,mm'}^{\sigma \sigma'}$. For simplicity, here we have assumed that the “off-diagonal blocks” of $n_{I,mm'}^{\sigma \sigma'}$ with $\sigma \neq \sigma'$ are much smaller in magnitude than the “diagonal blocks” with $\sigma = \sigma'$, and that the

eigenvalues obtained by diagonalizing $n_{I,mm'}^{\sigma\sigma'}$ separately for $\sigma = \uparrow, \downarrow$ do not differ appreciably from those obtained by diagonalizing the full local occupation matrix. Test calculations indicate that this is a rather good approximation. Subtracting the same double counting term as Eq. (7), we get the energy correction within SOC scheme as

$$\begin{aligned}\Delta E_{\text{DFT}+U} &= \frac{1}{2} \sum_I (U_I - J_I) \sum_{m\sigma} (\mathbf{n}_{I,\sigma m} - \mathbf{n}_{I,\sigma m} \mathbf{n}_{I,\sigma m}) \\ &= \frac{1}{2} \sum_I \bar{U}_I \sum_{\sigma} \left[\sum_m n_{I,mm'}^{\sigma\sigma} - \sum_{mm',\sigma'} n_{I,mm'}^{\sigma\sigma'} n_{I,m'm'}^{\sigma'\sigma} \right].\end{aligned}\quad (35)$$

The effective single-particle potential is given by

$$V_{I,mm'}^{\sigma\sigma'} = \bar{U}_I \left(1/2 \delta_{mm'} \delta_{\sigma\sigma'} - n_{I,mm'}^{\sigma\sigma'} \right). \quad (36)$$

Particularly, in this case, the Mulliken charge projector in Eq. (15) is generalized to a 2×2 tensor in the spin space,

$$\begin{aligned}\hat{P}_{I,mm'}^{\sigma\sigma'} &= \frac{1}{4N_{\mathbf{k}}} \sum_{\mathbf{k}} (|\tilde{\phi}_{\mathbf{k},\beta m'} \sigma'\rangle \langle \phi_{\mathbf{k},\beta m} \sigma| + |\phi_{\mathbf{k},\beta m'} \sigma'\rangle \langle \tilde{\phi}_{\mathbf{k},\beta m} \sigma| \\ &\quad + |\tilde{\phi}_{\mathbf{k},\beta m} \sigma\rangle \langle \phi_{\mathbf{k},\beta m'} \sigma'| + |\phi_{\mathbf{k},\beta m} \sigma\rangle \langle \tilde{\phi}_{\mathbf{k},\beta m'} \sigma'|).\end{aligned}\quad (37)$$

Thus, the local occupation matrix in SOC case becomes

$$\begin{aligned}n_{I,mm'}^{\sigma\sigma'} &= \frac{1}{N_{\mathbf{k}}} \sum_{\mathbf{n}\mathbf{k}} f_{n\mathbf{k}} \langle \psi_{n\mathbf{k}} | \hat{P}_{I,mm'}^{\sigma\sigma'} | \psi_{n\mathbf{k}} \rangle \\ &= \frac{1}{4N_{\mathbf{k}}} \sum_{\mathbf{k}} \sum_{\mu} \left(S_{\beta m,\mu}(\mathbf{k}) \rho_{\mu,\beta m'}^{\sigma\sigma'}(\mathbf{k}) \right. \\ &\quad \left. + \rho_{\beta m,\mu}^{\sigma\sigma'}(\mathbf{k}) S_{\mu,\beta m'}(\mathbf{k}) + S_{\beta m',\mu}(\mathbf{k}) \rho_{\mu,\beta m}^{\sigma'\sigma}(\mathbf{k}) \right. \\ &\quad \left. + \rho_{\beta m',\mu}^{\sigma'\sigma}(\mathbf{k}) S_{\mu,\beta m}(\mathbf{k}) \right).\end{aligned}\quad (38)$$

Within the scheme of two-component spinors, the density matrix becomes a 2×2 tensor in the spin space

$$\rho(\mathbf{k}) = \begin{bmatrix} \rho_{\mu\nu}^{\uparrow\uparrow}(\mathbf{k}) & \rho_{\mu\nu}^{\uparrow\downarrow}(\mathbf{k}) \\ \rho_{\mu\nu}^{\downarrow\uparrow}(\mathbf{k}) & \rho_{\mu\nu}^{\downarrow\downarrow}(\mathbf{k}) \end{bmatrix}, \quad (39)$$

where

$$\rho_{\mu\nu}^{\sigma\sigma'}(\mathbf{k}) = \sum_n f_{n\mathbf{k}} c_{n\mathbf{k},\mu}^{\sigma} c_{n\mathbf{k},\nu}^{\sigma*}. \quad (40)$$

Then, the effective single-particle potential operator becomes

$$\hat{V}_{\text{eff}}^{\sigma\sigma'}(\mathbf{k}) = \sum_I \sum_{mm'} V_{I,mm'}^{\sigma\sigma'} \hat{P}_{I,mm'}^{\sigma\sigma'}(\mathbf{k}), \quad (41)$$

where

$$\begin{aligned}\hat{P}_{I,mm'}^{\sigma\sigma'}(\mathbf{k}) &= \frac{1}{4} (|\tilde{\phi}_{\mathbf{k},\beta m'} \sigma'\rangle \langle \phi_{\mathbf{k},\beta m} \sigma| + |\phi_{\mathbf{k},\beta m'} \sigma'\rangle \langle \tilde{\phi}_{\mathbf{k},\beta m} \sigma| \\ &\quad + |\tilde{\phi}_{\mathbf{k},\beta m} \sigma\rangle \langle \phi_{\mathbf{k},\beta m'} \sigma'| + |\phi_{\mathbf{k},\beta m} \sigma\rangle \langle \tilde{\phi}_{\mathbf{k},\beta m'} \sigma'|).\end{aligned}\quad (42)$$

E. U and J parameters determined from the Yukawa potential

As shown in the previous sections, the Hubbard U and Hund J are two key parameters in DFT+ U calculations. They can be taken as empirical parameters or determined from pragmatic schemes, such as constrained DFT,^{23,48–50} constrained RPA,^{51–54} or linear-response approach.³⁰ In interacting many-electron systems, the Coulomb interaction between electrons is screened, resulting weaker and often shorter-ranged effective interactions. In principle, one could directly model such a screened Coulomb potential and directly use Eq. (3) to compute the U and J parameters. Previously, a simple form of such a screened potential—the Yukawa potential has been employed in the literature, and demonstrated to work reasonably well.^{57–59} In the present work, we follow such an approach and check how it works within our NAO-based DFT+ U scheme.

The Yukawa potential reads

$$v_{\text{sc}}(\mathbf{r}, \mathbf{r}') = \frac{e^{-\lambda|\mathbf{r}-\mathbf{r}'|}}{|\mathbf{r}-\mathbf{r}'|}, \quad (43)$$

where λ is a screening parameter. Compared to the bare Coulomb potential, the Yukawa potential decays exponentially fast to zero for large separations of two spatial points. Mathematically screened Coulomb interaction matrix elements based on the Yukawa potential given by Eq. (3) can be decomposed into two parts, i.e., an angular integral part involving spherical harmonics and a radial integral part called the Slater integrals,⁶¹ namely,

$$\langle mm' | v_{\text{sc}} | m'' m''' \rangle = \sum_{k=0}^{2l} a_k(m, m', m'' m''') F^{(k)}. \quad (44)$$

In Eq. (44),

$$\begin{aligned}a_k(m, m', m'' m''') &= \frac{4\pi}{2k+1} \sum_{q=-k}^k \int d\hat{\mathbf{r}} Y_{lm}^*(\hat{\mathbf{r}}) Y_{kq}(\hat{\mathbf{r}}) Y_{lm''}(\hat{\mathbf{r}}) \\ &\quad \times \int d\hat{\mathbf{r}}' Y_{lm'}^*(\hat{\mathbf{r}}') Y_{kq}^*(\hat{\mathbf{r}}') Y_{lm'''}(\hat{\mathbf{r}}')\end{aligned}\quad (45)$$

is the angular part that can be easily evaluated by Gaunt coefficients, and

$$F^{(k)} = \int \int R_l^2(r) v_{\text{sc}}^{(k)}(r, r') R_l^2(r') r^2 r'^2 dr dr' \quad (46)$$

is the radial part. The $v_{\text{sc}}^{(k)}(r, r')$ is the k -order coefficient of the expansion of $v_{\text{sc}}(\mathbf{r}, \mathbf{r}')$ by spherical harmonics,⁵⁹ i.e.,

$$v_{\text{sc}}(\mathbf{r}, \mathbf{r}') = \sum_{k=0}^{\infty} \frac{4\pi}{2k+1} v_{\text{sc}}^{(k)}(r, r') \sum_{q=-k}^k Y_{kq}^*(\hat{\mathbf{r}}) Y_{kq}(\hat{\mathbf{r}}'). \quad (47)$$

In case of the Yukawa potential form, $F^{(k)}$ in Eq. (46) is further reduced to

$$F^{(k)} = -(2k+1)\lambda \int \int R_l^2(r) j_k(i\lambda r_<) h_k^{(1)}(i\lambda r_>) R_l^2(r') r^2 r'^2 dr dr', \quad (48)$$

where j_k and $h_k^{(1)}$ are the spherical Bessel function and the spherical Hankel function of the first kind at order k , respectively. $r_>$

and $r_<$ are the smaller and the larger radius entering in the integral, i.e., $r_> = \max(r, r')$ and $r_< = \min(r, r')$. In this formulation, for a given set of local orbitals, the matrix elements of the screened Coulomb potential as given by Eq. (44), from which the U and J parameters can be extracted, depends only on the screening parameter λ . Thus, the problem of determining the U, J values becomes one for determining λ .

In the theory of Thomas–Fermi model, the screening parameter λ is a function of the charge density of the system

$$\lambda = 2 \left[\frac{3\rho}{\pi} \right]^{1/6}, \quad (49)$$

where ρ is the electron density. In this work, we use the effective screening parameter $\bar{\lambda}$ that is obtained by averaging the space-dependent screening parameter $\lambda(\mathbf{r})$,

$$\bar{\lambda} = \frac{\int \lambda(\mathbf{r}) \rho(\mathbf{r}) d\mathbf{r}}{\int \rho(\mathbf{r}) d\mathbf{r}}, \quad (50)$$

where the $\rho(\mathbf{r})$ is selected as the pseudo-charge density in the KS self-consistent iteration. This model provides us with a possible scheme of parameter-free DFT+ U with U and J determined in a self-consistent way.

For practical DFT+ U calculations, determining the U and J values based on the Yukawa potential brings simplification. First, in those DFT+ U schemes where the anisotropy forms of Coulomb interaction are used, two parameters, i.e., Hubbard U and Hund J , need to be determined, while in the Yukawa-potential approach only one parameter λ is needed. The screening parameter λ can be evaluated self-consistently with the help of the Thomas–Fermi screening model. Thus, a parameter-free DFT+ U scheme is, in principle, achievable. Second, for systems that have not been well investigated and no reference results are available, it is highly nontrivial to obtain the appropriate U and J values. Under such circumstances, a universal screening parameter λ in this approach can provide initial information for further investigation. Third, for accurate NAO-based calculations, there are often more than one radial function used for each d/f angular momentum channel. This raises the question if the Hubbard U correction need to be applied to all these d/f function channels and how to determine the U, J parameters for each individual orbital. Based on Eq. (44), the Yukawa potential approach allows one to conveniently determine the orbital-dependent U, J parameters, from which one can readily decide the relevant orbital channels where the Hubbard U correction is necessary.

III. COMPUTATIONAL DETAILS

Our DFT+ U implementation is carried out within the ABACUS code package.³⁶ In the present work, we use the SG15 optimized norm-conserving Vanderbilt (ONCV) multi-projector pseudo-potentials^{60–62} to describe the ion cores and optimized double- ζ plus polarization (DZP) atomic basis sets^{40,63} to expand the Kohn–Sham eigenfunctions. Within DZP, $4s2p2d1f$ atomic functions with a cutoff radius of 9 bohrs are used for the TM atoms and $2s2p1d$ atomic functions with r_{cutoff} of 7 bohrs for oxygen (O) atoms. In certain occasions, the triple- ζ plus polarization (TZDP) basis set with $5s3p3d2f$ for TMs and $3s3p2d$ for O are also used. For

Brillouin zone sampling, a Γ -inclusive $6 \times 6 \times 6$ \mathbf{k} -mesh is used. In band structure calculations, we set up \mathbf{k} -point paths explicitly along specified high-symmetry directions of the Brillouin zone. We consider ten high-symmetry points in \mathbf{k} -space for the rhombohedral Bravais lattice of type-II antiferromagnetic (AFM) structures (e.g., late TM monoxides MnO, FeO, CoO, and NiO). The corresponding \mathbf{k} -path is $\Gamma - L - B_1 | B - Z - \Gamma - X | Q - F - P_1 - Z | L - P$.⁶⁴ As for the case of simple tetragonal IrO₂, the \mathbf{k} -path is $\Gamma - X - M - \Gamma - Z - R - A - M$.⁶⁵ For all calculations, the Perdew–Burke–Ernzerhof (PBE) generalized gradient approximation (GGA) is used as the exchange-correlation functional⁶⁶ at the level of DFA, i.e., the PBE+ U scheme is employed in our test calculations below.

To validate our scheme and implementation, we make comparisons to several widely used software, including the LAPW method based code WIEN2k, Vienna *ab initio* simulation package (VASP), which is based on the PAW method, the Quantum-ESPRESSO (QE) package, which uses pseudopotential and plane-wave basis set,^{29,30} and LCAO based OpenMX code.^{44,67,68} For all calculations, we use the isotropic version of the simplified DFT+ U method, in which only the difference between Hubbard U and Hund J matters.⁵⁶ For all WIEN2k based calculations, we set the muffin-tin radii of TM atoms as 2.1 bohrs and that for O atoms as 1.4 bohrs. The convergence of the calculations is controlled by $R_{\text{MT}} \times K_{\text{max}} = 7.0$. In VASP calculations, we set the energy cutoff as 700 eV, and non-spherical contribution in gradient corrections inside the PAW sphere is included (LASPH = True.). In order to make comparisons, we use the same SG15 ONCV multi-projector pseudopotentials in QE calculations. The kinetic energy cutoffs for wavefunctions and charge density are 60 and 480 Ry, respectively. For OpenMX results, we simply cite those reported in Ref. 44.

The introduction of multiple radial functions (multiple- ζ) with the same angular momentum to the basis set in the LCAO framework makes it intricate to define the projector and, hence, the local subspace. The definition of the projector in Sec. II B indicates that the correlated sub-shell is not uniquely specified with only the correlated site I and angular momentum l because there is still a ζ index. In the present work, the DZP basis sets we are using contain two d -type functions and there is naturally the question regarding how to define the β index when constructing the projector [cf. Eqs. (15) and (33)]. In our current procedure^{40,63} to optimize the NAO basis sets, the first generated d function of TMs is most localized and represents best the local correlated subspace around the Fermi level. The estimated U and J parameters for these orbitals based on the Yukawa potential as described in Sec. II E also agree fairly well with those reported in the literature. In contrast, the second d function is rather delocalized and contributes little to the correlated subspace. As such, in the calculations reported below, the first d orbital is used to construct the projector. Further discussions about our choice and its efficacy will be discussed in Sec. IV E and the Appendix.

IV. RESULTS AND DISCUSSION

A. Bandgaps and magnetic moment

One of the most noteworthy successes of the DFT+ U approach is the reproducing of the observed insulating behavior of TMOs. In the standard DFT scheme, LDA and GGA either predict conducting behavior or yield gaps that are much smaller than the experimental

values. In TMOs, correlated valence d electrons tend to be localized due to strong on-site Coulomb interaction. Local and semi-local DFAs fail to describe this localization behavior. This deficiency is largely rectified by DFT+ U . Here, we apply our NAO-based DFT+ U implementation to prototypical Mott insulators, MnO, FeO, CoO, and NiO, and check how the obtained bandgaps vary with the \bar{U} value. We also compare our results with those produced by established computer codes, whereby the validity of our implementation can be demonstrated.

In our calculations, the NaCl-type structure is assumed for the four late TMOs—MnO, FeO, CoO, and NiO—where the chosen lattice constants are 4.445, 4.334, 4.254, and 4.171 Å, respectively.⁶⁹ For all these four systems, we consider the type-II AFM structure, where the AFM order is along the (111) direction.^{30,59,70} The SOC effect is not considered for these systems.

Table I presents the calculated gaps as a function of the effective on-site Coulomb interaction parameter \bar{U} . Without the U correction, PBE yields zero gaps for FeO and CoO and significantly underestimates the bandgaps for MnO and NiO. When the U correction is applied, the obtained bandgap opens up and steadily increases with an increasing \bar{U} value, as expected. When \bar{U} reaches a physically meaningful value of about 6 eV, our calculated PBE+ U bandgaps show a fairly good agreement with the experimental values for all four TMOs.

Since different projectors and numerical frameworks are used in different computer codes, the calculated DFT+ U bandgaps could differ noticeably even with the same U value. However, the results should be qualitatively similar. For instance, the calculated DFT+ U bandgaps should follow a similar trend as the U value increases. To check this, in **Fig. 1**, we present the bandgaps for the four TMOs as a function of \bar{U} , as obtained by five computer codes: ABACUS, OpenMX, VASP, WIEN2k, and QE. The OpenMX results for all the four systems are taken from Ref. 44, where LDA functional was used. For all other codes, the PBE functional is used in DFT+ U calculations. We do not expect using PBE instead of LDA will produce significant difference for the curves presented in **Fig. 1**. For MnO, the results of VASP, WIEN2k, and QE are taken from Ref. 70, whereas the results for other TMOs are calculated in the present work. **Figure 1** indicates the bandgaps obtained from different codes follow the same trend as \bar{U} increases, but the obtained bandgaps can differ by as large as 1 eV for the same \bar{U} value. This means that the

TABLE I. Bandgaps (in eV) of MnO, FeO, CoO, and NiO as a function of effective on-site Coulomb energy \bar{U} (in eV). The experimental values are presented in the last row.

\bar{U} (eV)	MnO	FeO	CoO	NiO
0.0	1.13	0.00	0.00	0.64
2.0	1.65	0.76	1.84	1.88
4.0	1.98	2.44	2.57	2.60
6.0	2.18	2.62	3.07	3.21
Expt.	3.6–3.8 ^a	2.4 ^b	2.4 ^c	4.0, ^d 4.3 ^e

^aReference 71.

^bReference 72.

^cReference 73.

^dReference 74.

^eReference 75.

“best” \bar{U} value to reproduce the experimental results varies for different numerical frameworks. Compared to other codes, ABACUS displays a rather “normal” behavior, which is a strong evidence of the validity of our projector scheme and numerical implementations.

The local magnetic moment of TM atoms within MnO, FeO, CoO, and NiO is also calculated by ABACUS, and the results are presented in **Table II**. **Table II** shows the expected trend that the local magnetic moments get enhanced with increasing \bar{U} . With physical \bar{U} values, the obtained PBE+ U magnetic moments show an overall good agreement with experimental results and previously reported theoretical results.^{23,44}

B. Projected density of states and band structures

To gain more insights into the performance of our DFT+ U scheme, we calculate the projected density of states (PDOS) and band structures of MnO, FeO, CoO, and NiO at a fixed effective on-site Coulomb interaction parameter \bar{U} of 5.0 eV, and the obtained results are plotted in **Figs. 2** and **3**, respectively. In the type-II AFM unit cells, the spin polarizations of the two neighboring TM atoms are of the same magnitude but anti-parallel in direction. In **Fig. 2**, we project the total density of states (TDOS) to the spin-up polarized TM atoms and their nearest oxygen atoms. **Figure 2(a)** indicates that 3d electrons of the projecting site Mn are nearly fully spin-up polarized, which suggests all 3d electrons occupy the spin up states, and this result agrees with the previous work using WIEN2k, VASP, and QE codes.⁷⁰ As the number of d electrons increases from Mn to Ni, the spin-down d states also get populated, resulting in a decrease of the total magnetic moments (cf. **Table II**). In all four mono-oxides, there are significant hybridizations between the O 2p and TM 3d orbitals over a wide range of energy. In particular, the top valence states have a predominant contribution from the O 2p orbitals, suggesting a charge transfer character of these TMOs. Such behaviors agree with the chemistry bond theory and previous theoretical results.^{23,30,44,70}

We further present the calculated band structures of the four TMOs in **Fig. 3**, which display the typical character of strongly correlated systems. The occupied manifold of the KS states is a mixture of the O 2p and TM 3d characters. Energetically, the TM 3d dominating bands sit below the O 2p dominating ones due to the fact that the strong Coulomb repulsion pushes the occupied TM 3d states deeply down in energy. Furthermore, when going from MnO to NiO, a part of the low conduction bands transfers into the valence bands, while maintaining an insulating bandgap of about 3 eV [cf. **Figs. 3(a)** and **3(d)**]. Both the top valence bands and bottom conduction bands show a very small dispersion of the order of 1.0 eV, which is much smaller when compared to the effective on-site Coulomb interaction energy \bar{U} . Theoretically, the hopping amplitude of electrons between neighboring lattice sites is proportional to the bandwidth. In the cases where the bandwidth is much smaller than the on-site Coulomb interactions, the transport process of the valence electrons gets hampered and it is very difficult for them to hop between neighboring sites, and then 3d electrons become localized, leading to the insulating behavior. The narrow widths of the top valence bands agree well with this physics picture of strongly correlated systems. All these properties suggest that our DFT+ U implementation successfully captures the fundamental physical mechanism of strongly correlated TM monoxides.

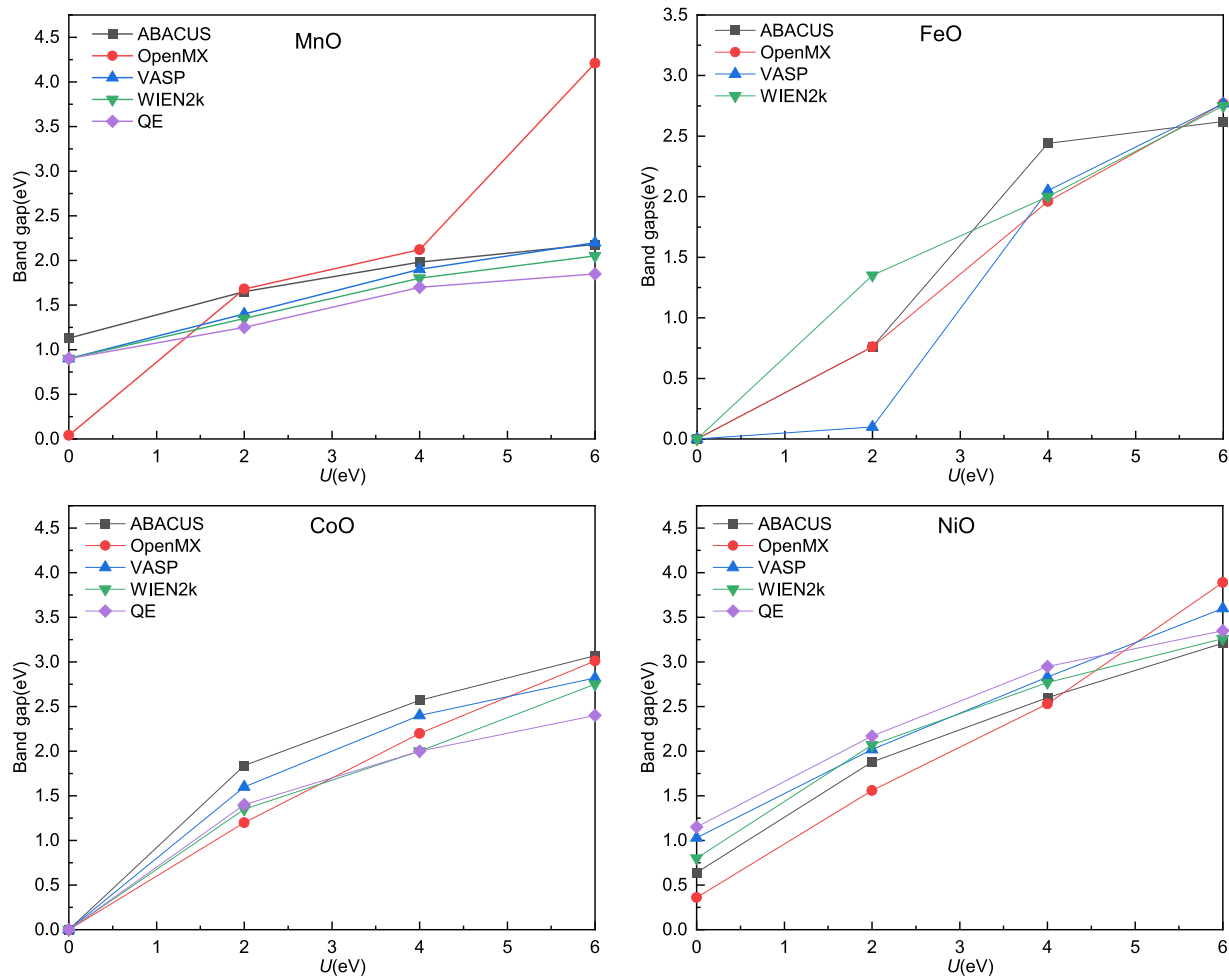


FIG. 1. Bandgaps of MnO, FeO, CoO, and NiO as a function of \bar{U} as calculated by different computer codes. The rhombohedral unit cell with type-II AFM structure is used. For FeO, we could not obtain stable self-consistent results for all \bar{U} values with QE, and hence the QE results are not included in the FeO panel. The LDA+ U results taken from Ref. 44 are presented for OpenMX, whereas, for all other codes, the PBE+ U results are presented.

TABLE II. Magnetic moments (in μ_B) of TM atoms within the four TMOs as a function of effective on-site Coulomb energy \bar{U} .

\bar{U} (eV)	MnO	FeO	CoO	NiO
0.0	4.39	3.44	2.47	1.21
2.0	4.64	3.60	2.56	1.53
4.0	4.74	3.70	2.69	1.64
6.0	4.80	3.77	2.74	1.71
Expt.	4.58, ^a 4.79 ^b	3.32 ^c	3.8, ^c 3.35 ^d	1.90, ^a 1.77 ^b
Theo.	4.61 ^e	3.62 ^e	2.63 ^e	1.69, ^e 1.74 ^f

^a Reference 76.

^b Reference 77.

^c Reference 78.

^d Reference 79.

^e Reference 23.

^f Reference 44 ($U = 6.0$ eV).

As a comparison to another implementation scheme, Fig. 4 presents the PBE+ U band structures of NiO calculated by ABACUS and the plane-wave based code QE at \bar{U} of 5.0 eV. The DFT+ U bands of NiO given by the two codes are fairly close, with the occupied d bands of ABACUS slightly lower in energy compared to the QE results. This difference stems from the different underlying DFT and DFT+ U implementation schemes of the two codes. First, the basis sets used in the two codes are different. ABACUS employs the NAO basis sets whereas the plane-wave basis sets are used in QE. This already yields noticeable differences in the PBE band structure of NiO. Second, the local correlated orbitals used to define the DFT+ U projector are different for the two codes. The most localized d or f NAOs are used as the local correlated orbitals in the ABACUS while the atomic pseudo-wave-functions are used in QE.³⁰ These two atomic-like orbitals differ in shape and cutoff radii in real space. This can induce non-negligible difference in the DFT+ U results even if the same \bar{U} value is used.

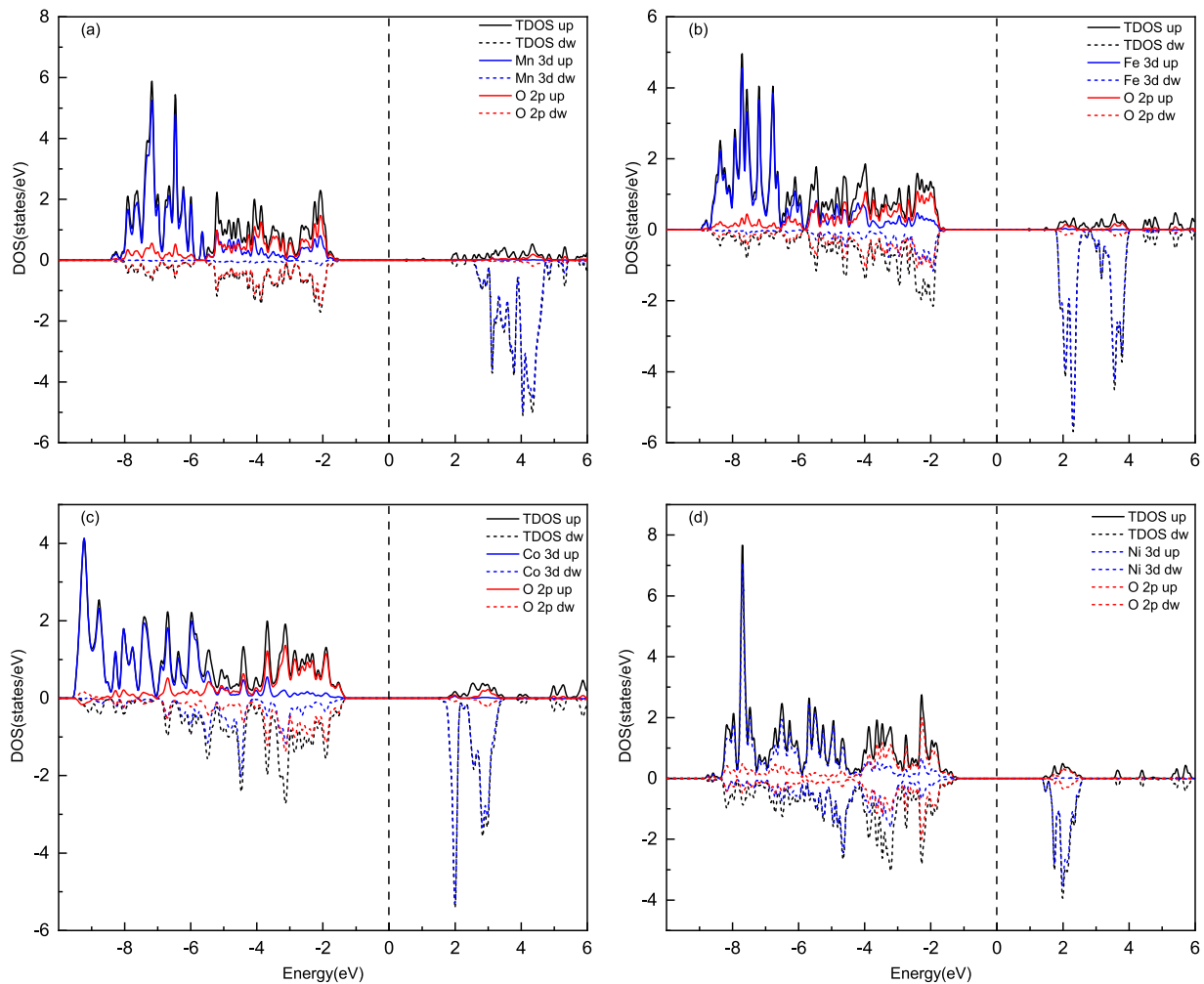


FIG. 2. The TDOS and PDOS of spin-up polarized TM atom and its nearest O atom of MnO, FeO, CoO, and NiO calculated with \bar{U} of 5 eV are depicted in (a)–(d), respectively. The zeroes of the energy axes are set to be the Fermi level (vertical dashed line). The upper and lower panels correspond to the up-spin and down-spin channels.

C. Validation of the force and stress implementations

To assess the validity of our DFT+ U force and stress implementations, we compare the results calculated via the analytical derivative formalism in Eqs. (25) and (30) with those obtained by the finite-difference (FD) method, taking NiO in the conventional cell as the testing system. We first calculate the atomic forces for a series of structures with the Ni atom moving along the z -axis while other atoms staying at their original positions, and the results are reported in Table III. As clearly shown in Table III, the forces based on analytical gradients and those determined by the FD method agree fairly well, with the remaining discrepancy below 2%.

For benchmark stress calculations, we fix the lattice constants a and b and vary the length of c of the NiO (conventional cubic) cell, and the results are presented in Table IV. Comparison of the FD and

analytical stress results shows that the relative deviations are in the order of 2%–3%.

There are two reasons that have contributed to the discrepancy between the analytical and finite-difference forces and stresses. The first reason is that higher-order derivatives are contained in the FD forces and stresses, whereas only linear terms are present in the analytical ones. The second reason is that some of the involved integrals are computed using the quadrature method. The derivatives of the quadrature grid weights are not included in the analytical force and stress calculations. Therefore, the above noted about 2% discrepancy can be further reduced by decreasing the increment in the FD calculations and/or using tighter quadrature grids (corresponding to higher energy cutoff in ABACUS calculations). The accuracy noted above is what one typically has in production calculations

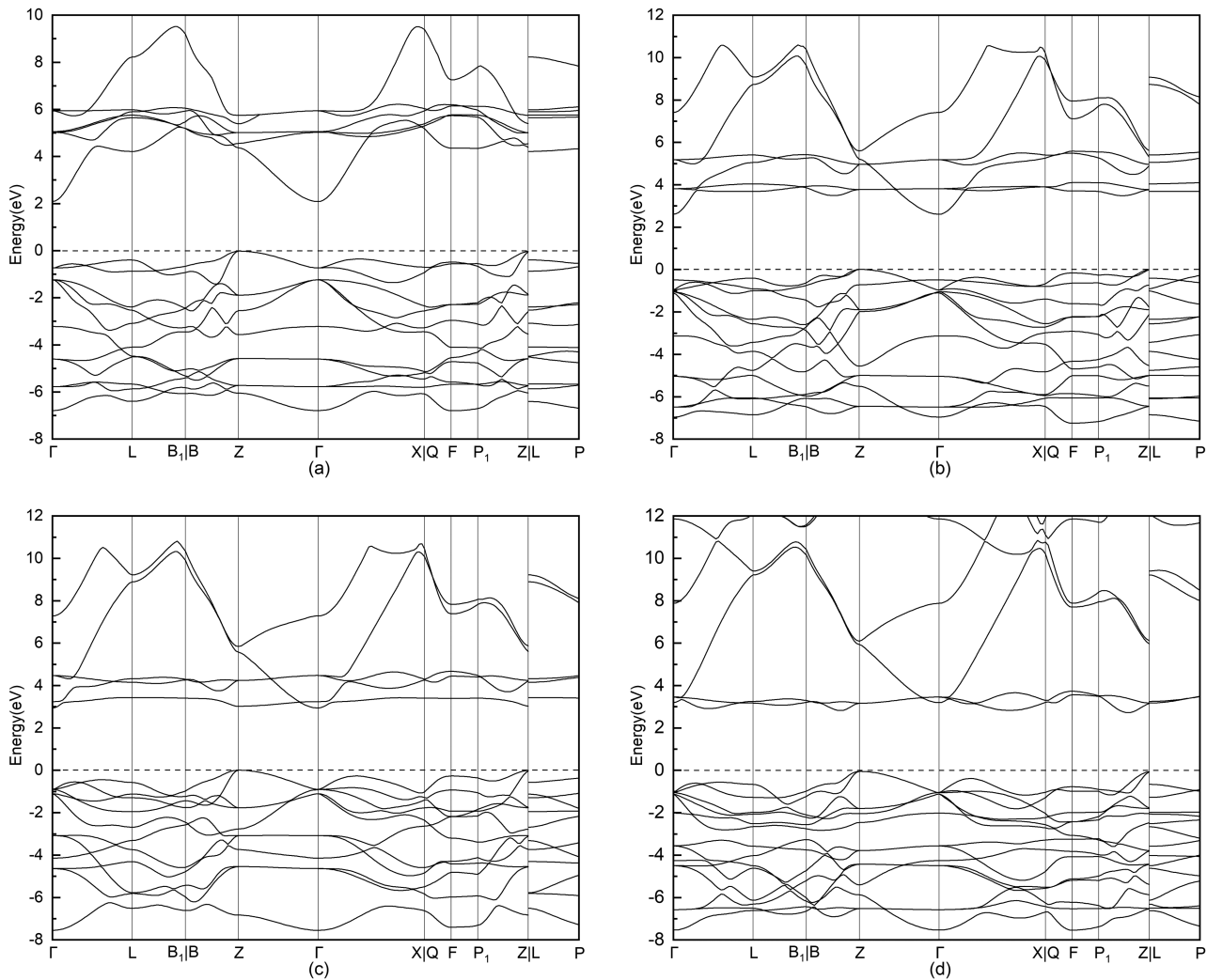


FIG. 3. The ABACUS PBE+U band structures of MnO, FeO, CoO, and NiO calculated with \bar{U} of 5.0 eV are depicted in panels (a)–(d), respectively. The energy zero is set to be the top of the occupied bands (horizontal dashed line).

and is usually adequate for practical purposes, such as geometry relaxations.

D. DFT+U+SOC band structure

The strength of SOC scales as $O(Z^4)$, where Z is the atomic number. The atomic number of iridium (Ir) is 77, which is nearly three times larger than that of Mn (atomic number 25). Thus, theoretically, the SOC effect of Ir-based compounds is much stronger than 3d TM materials. In this subsection, we examine the band structure of IrO₂ to assess the performance of our DFT+U+SOC implementation. We consider the AFM structure with the magnetic momenta of two neighboring Ir atoms in the conventional cell antiparallel along the z -axis. The DFT+U correction is applied to the 5d electrons of Ir atoms with $\bar{U} = 2.0$ eV. The calculated PBE+U

and PBE+U+SOC band structures are presented in Figs. 5(a) and 5(b), respectively.

The PDOS analysis (not shown) suggests that the main components of the bands located in the energy window included in Fig. 5 are 5d electrons of the Ir atom. Comparing Figs. 5(a) and 5(b), the originally degenerate bands along the k -path from Z to A are split into sub-bands after the introduction of SOC, which is the typical effects of SOC on heavy elements.

For comparison, in Fig. 5(c), the PBE+U+SOC band structure calculated by VASP is also presented. As can be seen, ABACUS and VASP give similar band structures for IrO₂. The small difference in details between ABACUS [Fig. 5(b)] and VASP [Fig. 5(c)] results may stem from different basis sets, different pseudopotentials, and the different DFT+U and SOC schemes. In the latter case, in VASP, the SOC is included in a non-self-consistent way based on

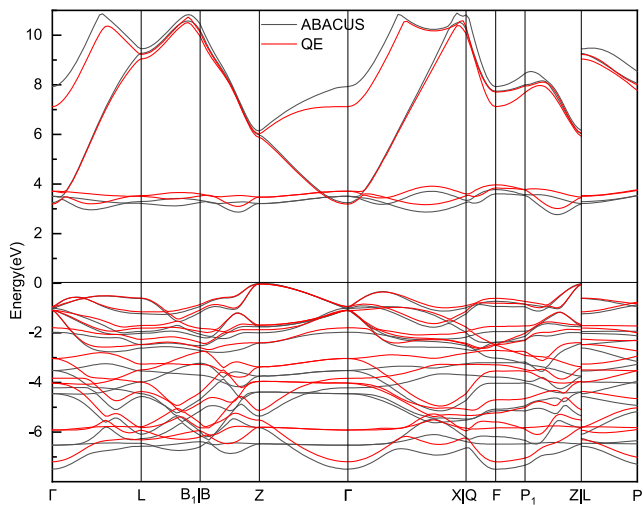


FIG. 4. The PBE+U band structures of NiO calculated by ABACUS and QE with $U = 5$ eV. The zeroes of energy are set to be the top of highest occupied bands.

a perturbation approach, whereas in ABACUS, the SOC is treated in a self-consistent way. In addition, the results in Fig. 5 are in good agreement with previous theoretical work using all-electron full-potential DFT+U+SOC and LDA+DMFT methods.⁶⁵

TABLE III. Benchmark force calculations for NiO. The first column is the z coordinate of the Ni atom, and the second column shows the energy increase for each move of the Ni atom. The third and fourth columns present the FD and analytical forces (in eV/Å) experienced by the Ni atom, respectively. The last column presents the relative deviations (in percentage) of the results computed by the two approaches.

z (Å)	ΔE (eV)	$\Delta E/\Delta z$	Force	Deviation (%)
2.297 820			-2.563 364	
2.301 998	0.010 869	-2.601 461	-2.637 573	1.37
2.306 175	0.011 193	-2.679 244	-2.712 991	1.24
2.310 353	0.011 472	-2.745 873	-2.789 429	1.56
2.314 531	0.011 831	-2.831 828	-2.868 811	1.29

TABLE IV. Benchmark stress calculations for NiO. The first column is the length of the lattice constant c of the conventional unit cell, and the second column shows the energy change of each increase of c . The third and fourth columns present the FD and analytical stress results (in kbar), respectively. In the third column, the FD stress is calculated by $\Delta E/\varepsilon\Omega$, where ε is the strain component of c direction, i.e., ε_{cc} and Ω is the cell volume.

c (bohr)	ΔE (eV)	$\Delta E/\varepsilon\Omega$	Stress	Deviations (%)
7.895 000			-47.484 882	
7.902 895	0.002 266	-52.926 873	-51.879 179	-2.02
7.910 790	0.002 464	-57.497 658	-56.164 020	-2.37
7.918 685	0.002 666	-62.141 370	-60.327 858	-3.01
7.926 580	0.002 842	-66.188 954	-64.360 639	-2.84

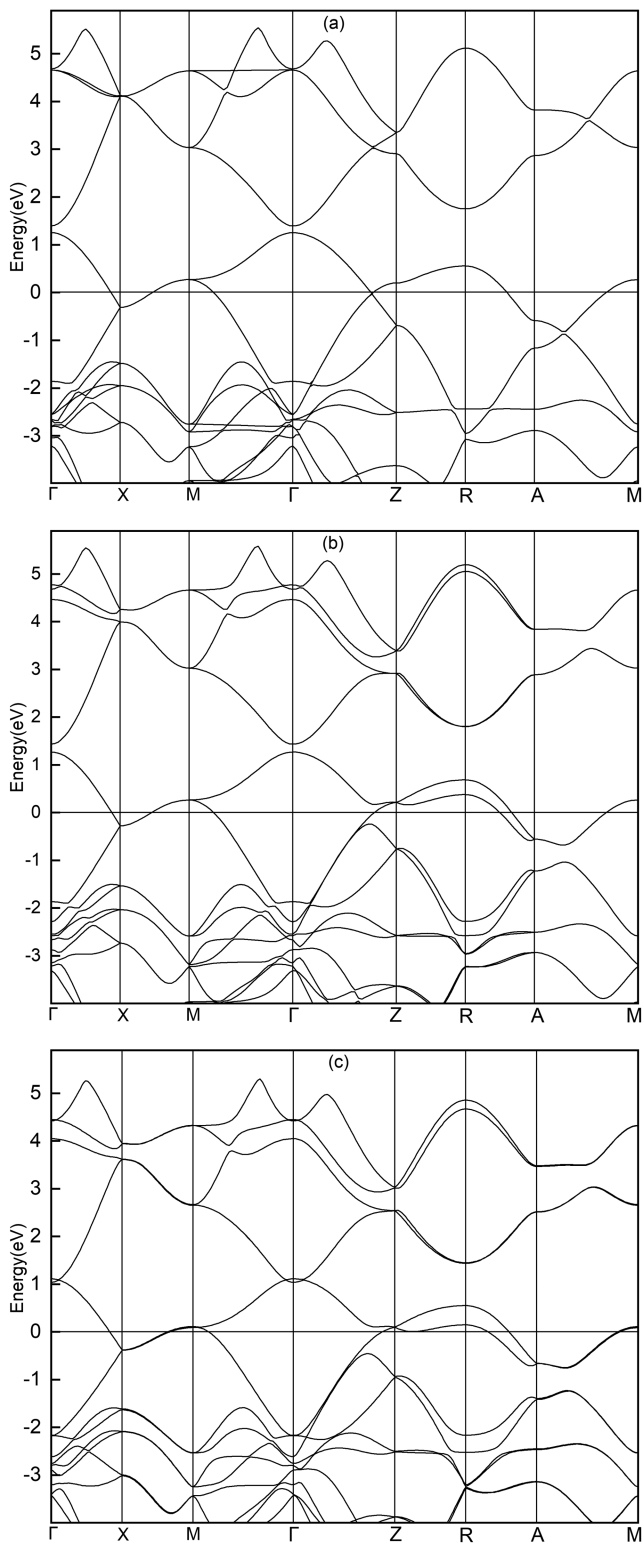


FIG. 5. Band structures of IrO_2 calculated by (a) ABACUS DFT+U, (b) ABACUS DFT+U+SOC, and (c) VASP DFT+U+SOC schemes.

E. Yukawa-potential based U and J parameters

In the above discussions, we focused on the validation of our DFT+ U implementation, where U and J are treated as given parameters. To apply DFT+ U to novel materials where no reference results are available, it is crucial to be able to determine these parameters from first principles calculations. As mentioned earlier, in the literature, different theoretical schemes have been developed to determine these parameters.^{23,30,50–54} In this subsection, we check how the scheme based on the Yukawa potential, as described in Sec. II E, works for determining U, J parameters.

As discussed in Sec. II E, for a given set of NAO basis functions, the calculated interaction parameters based on Eq. (44) depend solely on the screening parameter λ . Here, we first examine how the Coulomb interaction parameter U and the exchange parameter J change with the λ value for the local d/f -type orbitals. We take three TMOs, i.e., MnO, FeO, and NiO, as test examples and use NAO DZP basis sets in the calculations. For the TMs Mn, Fe, and Ni, the DZP basis set contains two d functions and one f function. The Yukawa potential scheme allows one to readily compute the U, J parameters for all these orbital functions.

Table V presents the calculated U and J parameters for the two d and one f orbitals with λ varying from 0.80 to 1.08 bohr⁻¹. First, one can see that the U, J values for the first d orbital are one order of magnitude larger than those for the second one. This is because the first d orbital is localized and has no node, whereas the second orbital, designed to be orthogonalized to the first one, is much more extended and has a node (see the Appendix for further details). Thus, it is not surprising that the U, J corresponding to the second d orbital are much smaller than those of the first one. According to **Table V**, one can see that the second d orbital can be safely excluded from the correlated subspace in the DFT+ U calculations. Furthermore, for these TM compounds, the f functions are “polarized orbitals” and represent orbital space that is well separated from the correlated

subspace around the Fermi level and, consequently, require no special treatment. Consistent with this, the U, J parameters for the f orbital are also significantly smaller than those of the first d orbital.

Table V shows that the obtained U, J values steadily decrease upon increasing the λ value, which is easy to understand since a larger λ means a stronger screening of the Coulomb interaction. Focusing on the first d orbital ($d1$ in **Table V**) and comparing to the results given by constrained DFT,⁸⁰ constrained RPA,⁵⁴ and local screened Coulomb correction (LSCC) scheme,⁵⁹ we find that a screening parameter λ around 1.00 bohr⁻¹ yields U, J values that are fairly close to those reported in the literature. Remarkably, it seems that $\lambda \approx 1$ bohr⁻¹ is a sensible choice that works well for all three TMOs. Therefore, at least the TM compounds, our DFT+ U scheme together with the Yukawa-potential scheme for determining U, J parameters can be viewed as a semi-empirical approach that has predictive power; namely, the only input parameter is fixed and does not vary for different materials.

Although a $\lambda = 1.00$ bohr⁻¹ seems to work well for all TMOs, we do not expect it to work in general cases because a fixed λ value means that the obtained U, J values only depend on the atomic species and the chosen NAO basis sets but not on the chemical environment. For a generally applicable scheme, λ should reflect the chemical environment of the system. The averaged $\bar{\lambda}$ introduced in Eq. (50) depends on the electron density of the system via the Thomas–Fermi screening model and, thus, accounts for the chemical environment in a natural way. In Ref. 59, it has been shown that such a scheme (termed LSCC there) yields rather good U, J values within the LAPW framework. Note that, within such a scheme, the averaged screening parameter $\bar{\lambda}$ varies during the self-consistent iterations and hence so do the U, J values, until the convergence is reached. We also implemented the LSCC scheme in ABACUS, and the self-consistently determined $\bar{\lambda}$ values for MnO, FeO, CoO, and NiO are 1.581, 1.627, 1.649, and 1.677 bohr⁻¹, respectively. However, the $\bar{\lambda}$ parameters lead to too short screening

TABLE V. On-site Coulomb energy U and exchange energy J (in eV) as a function of screening parameter λ (in bohr⁻¹) for MnO, FeO, and NiO in DZP basis. Here, d and f are angular momentum indices while the number behind them are multiplicity indices ζ .

λ	MnO						FeO						NiO					
	$d1$		$d2$		$f1$		$d1$		$d2$		$f1$		$d1$		$d2$		$f1$	
	U	J	U	J	U	J	U	J	U	J	U	J	U	J	U	J	U	J
0.80	6.62	1.00	0.62	0.20	2.93	0.49	7.41	1.08	0.57	0.20	2.80	0.48	8.04	1.20	0.49	0.20	2.29	0.44
0.84	6.35	1.00	0.57	0.19	2.77	0.48	7.12	1.07	0.53	0.19	2.65	0.48	7.74	1.19	0.45	0.19	2.16	0.44
0.88	6.09	0.99	0.53	0.18	2.62	0.47	6.84	1.06	0.49	0.18	2.51	0.47	7.44	1.18	0.42	0.18	2.04	0.43
0.92	5.85	0.98	0.50	0.18	2.48	0.47	6.58	1.05	0.46	0.18	2.38	0.46	7.16	1.17	0.39	0.18	1.93	0.42
0.96	5.62	0.97	0.47	0.17	2.36	0.46	6.33	1.04	0.43	0.17	2.26	0.46	6.90	1.16	0.36	0.17	1.82	0.42
1.00	5.40	0.96	0.44	0.16	2.24	0.45	6.10	1.03	0.40	0.16	2.14	0.45	6.65	1.15	0.34	0.16	1.73	0.41
1.04	5.20	0.95	0.41	0.16	2.13	0.45	5.87	1.03	0.38	0.16	2.04	0.44	6.41	1.15	0.32	0.16	1.64	0.40
1.08	5.00	0.94	0.39	0.15	2.03	0.44	5.66	1.02	0.35	0.15	1.94	0.44	6.18	1.14	0.30	0.15	1.56	0.40
cDFT ^a	$U = 4.7, J = 0.8$						$U = 4.8, J = 0.9$						$U = 5.2, J = 0.9$					
cRPA ^b	$U = 5.5, J = 0.6$						$U = 5.7, J = 0.7$						$U = 6.6, J = 0.7$					

^aThe results of constrained DFT implemented in LAPW framework from Ref. 80.

^bThe results of constrained RPA in maximally localized Wannier functions from Ref. 54.

TABLE VI. The energy differences (in meV) between the AFM and FM states of four materials calculated by PBE and PBE+ U with U and J determined with a scaled screening parameter (see the text), and compared to the experimental values and the calculated results reported in Ref. 59. In LSCC, the U , J parameters are obtained without rescaling the $\bar{\lambda}$ parameter whereas in our work, a scaling factor of 0.625 is used.

	PBE (this work)	PBE ⁵⁹	LSCC ⁵⁹	PBE+ U (this work)	Expt.
MnO	-157.3	-152	-99.8	-84.5	-62 ⁸¹
NiO	-258.2	-261	-107	-145.4	-112 ⁸²
MnF ₂	-64.6	-60.5	-28.3	-22.2	-15.2 ⁸³
NiF ₂	-85.9	-69.6	-20.1	-31.7	-13.8 ⁸³

lengths for our NAO basis sets and the calculated U , J values are too small. In practice, we find that introducing a scaling factor of 0.625 can reduce the $\bar{\lambda}$ value to a range (around 1.0 bohr⁻¹) that yields physically reasonable U , J values. The reason that an additional scaling factor is needed here, compared to the original LAPW-based LSCC implementation, is that the local NAOs used here is more extended than the local orbitals in the LAPW framework, which are restricted within the muffin-tin sphere. Hence, the computed interaction parameters within the NAO framework will be smaller than the LAPW case if the same screening parameter is used.

In Table VI, we present the energy differences between the AFM and ferromagnetic (FM) states of four materials, as computed by PBE and PBE+ U . The experimental results and the results reported in Ref. 59 are included for comparison. The PBE+ U with a scaled $\bar{\lambda}$ parameter, obtained from the Thomas–Fermi model, yields results that show satisfactory agreement with experiment and the LSCC results. The accuracy of the results is a factor of two better than that of PBE.

V. SUMMARY

We present a detailed formulation of the DFT+ U method within the framework of NAO basis set. The key in this formulation is to use a symmetrized Mulliken charge projector, constructed in terms of the most localized d or f orbital basis functions, to project a correlated local subspace out of the full KS orbital space. We implemented such a scheme within the ABACUS code package, and our implementation allows not only self-consistent electronic structure calculations with or without including the SOC effect but also enables force and stress calculations. The efficacy of our formalism and implementation has been demonstrated for the prototypical TMOs and IrO₂. Furthermore, we tested the scheme for computing the U , J parameters based on a screened Yukawa potential, and found that, while a fixed screening parameter works for all TMOs, determining such a parameter from the electron density via the Thomas–Fermi model leads to an underestimation of the U , J values. However, this issue can be fixed by introducing a universal rescaling parameter to increase the screening length. We believe that the experience gained in the present work will be very helpful for developing Hubbard-type local correction scheme within the atomic-orbital basis set framework.

ACKNOWLEDGMENTS

This work was supported by the National Natural Science Foundation of China (Grant Nos. 12134012, 11874335, and 21873005) and the Strategic Priority Research Program of Chinese Academy of Sciences (Grant No. XDPB25). We thank Dr. Wenshuai Zhang for generating the optimized NAO basis sets used in the present work, available at the official ABACUS website.⁸⁴ Parts of the calculations are done on the supercomputing system in the Supercomputing Center of USTC.

AUTHOR DECLARATIONS

Conflict of Interest

The authors declare that they have no conflicts of interest.

Author Contributions

Xin Qu: formal analysis (equal); investigation (equal); methodology (equal); software (equal); writing – original draft (lead); writing – review & editing (equal). **Peng Xu:** Supervision (supporting); writing – review & editing (equal). **Hong Jiang:** Conceptualization (equal); methodology (equal); supervision (equal); writing – review & editing (equal). **Lixin He:** Conceptualization (equal); funding acquisition (equal); methodology (equal); software (equal); supervision (equal); writing – review & editing (equal). **Xinguo Ren:** Data curation (equal); formal analysis (equal); investigation (equal); methodology (equal); project administration (equal); resources (equal); software (equal); supervision (equal); validation (equal); writing – original draft (equal); writing – review & editing (equal)

All authors read and approved the final manuscript.

DATA AVAILABILITY

The data that support the findings of this study are available from the corresponding author upon reasonable request.

APPENDIX: THE INFLUENCE OF THE CHOICE OF LOCAL ORBITALS ON DFT+ U

In this appendix, we investigate two issues about employing the local atomic orbitals to construct the projector within the NAO basis set framework, which have not been elaborated in the main text. The first issue, which has already been mentioned in Sec. IV E, is whether all basis orbitals belonging to characteristic d/f angular moment channel need to be included in the DFT+ U correction. The second issue is the influence of the shape of the local orbitals on the DFT+ U results.

To address the first question, we perform a partial occupation analysis of the d orbitals, taking MnO as an example. Table VII presents the local occupation numbers of all Mn d orbitals of MnO, as given by Eq. (16). For completeness, both DZP and TZDP basis sets have been used, and in the latter case, there are three d orbitals for Mn. From Table VII, it can be clearly seen that local occupation numbers of the second or third d orbital are significantly smaller than the first d one. This means that the second or third d orbitals contribute little to the top valence states, and the majority of the correlated local subspace is described by the first d orbital. From

TABLE VII. Partial occupation numbers (sum of spin-up and spin-down channels) of Mn d orbitals of MnO as calculated by PBE. Results obtained using DZP (two d orbitals) and TZDP (three d orbitals) are presented.

	d_{xy}	d_{xz}	d_{z^2}	d_{yz}	$d_{x^2-y^2}$
DZP	Zeta = 1	1.372	1.372	0.773	1.372
	Zeta = 2	0.012	0.012	0.007	0.012
TZDP	Zeta = 1	1.355	1.343	0.728	1.474
	Zeta = 2	0.030	0.032	0.028	0.002
	Zeta = 3	0.002	0.002	-0.006	0.002
					-0.006

the point of view of real-space locality, the first (and innermost) d orbital, i.e., zeta 1 in Table VII, is most localized and has no node. The other d orbitals are designed to be orthogonal to the first one, so that they have nodes and are more delocalized (cf. Fig. 6). Such

behavior is also reflected in two-electron integrals of the screened Coulomb potential. As is shown in Table VI, the on-site Coulomb interaction and exchange energies of the second d orbital are smaller by one order of magnitude compared to the first d one. Both the orbital occupation and interaction parameter analyses suggest that we can most likely neglect the on-site Coulomb correction to the second or higher d orbital.

Despite the observation that most probably one only needs to apply the Hubbard U correction to the most localized orbital for multi-zeta NAO basis sets, we nevertheless also checked what if the U correction is added to all d orbitals. In Fig. 6, the PDOS of NiO by using DZP and TZDP basis set on the spin-up polarized nickel atoms and their nearest oxygen atoms are shown. Figures 6(a) and 6(c) are the results of standard DFT+ U , where \tilde{U} is set to be 5.5 eV and the on-site Coulomb interaction correction is only applied to the first d orbitals. For comparison, we then apply on-site Coulomb

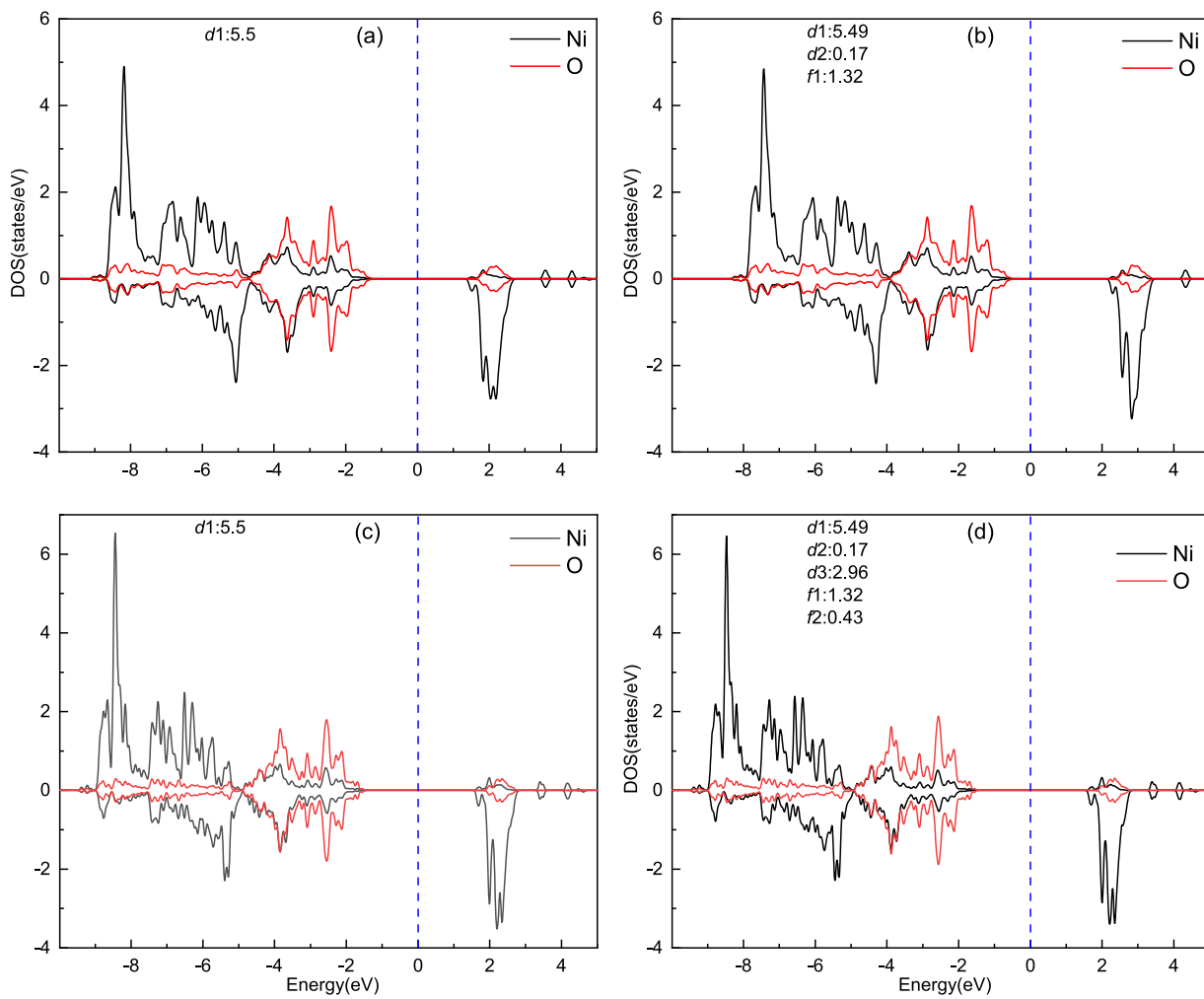


FIG. 6. Projected DOS of NiO where different on-site Coulomb interactions are employed to different d/f orbital: (a) and (b) DZP basis, (c) and (d) TZDP basis. The upper and lower panels correspond to up-spin and down-spin. The zero of energy is set to be Fermi level (vertical dashed line).

interaction corrections to all d and polarization f orbitals where the corresponding \hat{U} value is determined by the Yukawa potential scheme, as described in Sec. II E, with the screened parameter λ fixed at 1.00 bohr $^{-1}$. The obtained results are depicted in Figs. 6(b) and 6(d) for the DZP and TZDP basis sets, respectively. In Fig. 6, the label $d/f - i$ means the i -th d/f orbital and the values behind them are the corresponding \hat{U} values. As shown in Fig. 6, the PDOS results undergo little changes for both DZP and TZDP basis sets if the U corrections are added to all d and polarization f orbitals. This result validates our DFT+ U projection scheme that only the first, most localized correlated orbital needs to be included in the construction of the projector.

Finally, we briefly discuss the possible influence of the shape of the local atomic orbitals used in the projector construction on the DFT+ U calculations. From the discussion in Sec. II A, one can see that the KS wavefunctions and the local orbitals control the local

occupation matrix and, hence, directly affect the results of DFT+ U calculations. Since all properly worked DFT codes must yield nearly the same wavefunctions in real space, provided that the same pseudopotential is used, the DFT+ U results mainly depend on the choice of local correlated orbitals. In Fig. 7, we plot the radial functions of Mn d orbitals of the DZP basis sets, employed in ABACUS (upper panel) and OpenMX (lower panel) calculations. For both codes, the first Mn d orbitals (the nodeless ones) are localized within 1.5 Å around the nucleus, with a sharp peak positioned around $r = 0.5$ Å. The local occupation numbers given by the Mulliken charge projector in OpenMX are 1.447 for t_{2g} orbitals and 0.412 for e_g orbitals, in comparison to 1.372 and 0.773 as given by ABACUS (cf. Table VII). Such difference is a manifestation of the difference in the radial shape of the first d functions between the two codes, as plotted in Fig. 7. As such, the DFT+ U implementations in ABACUS and OpenMX yield qualitatively similar but quantitatively noticeably different results, as demonstrated in Fig. 1.

REFERENCES

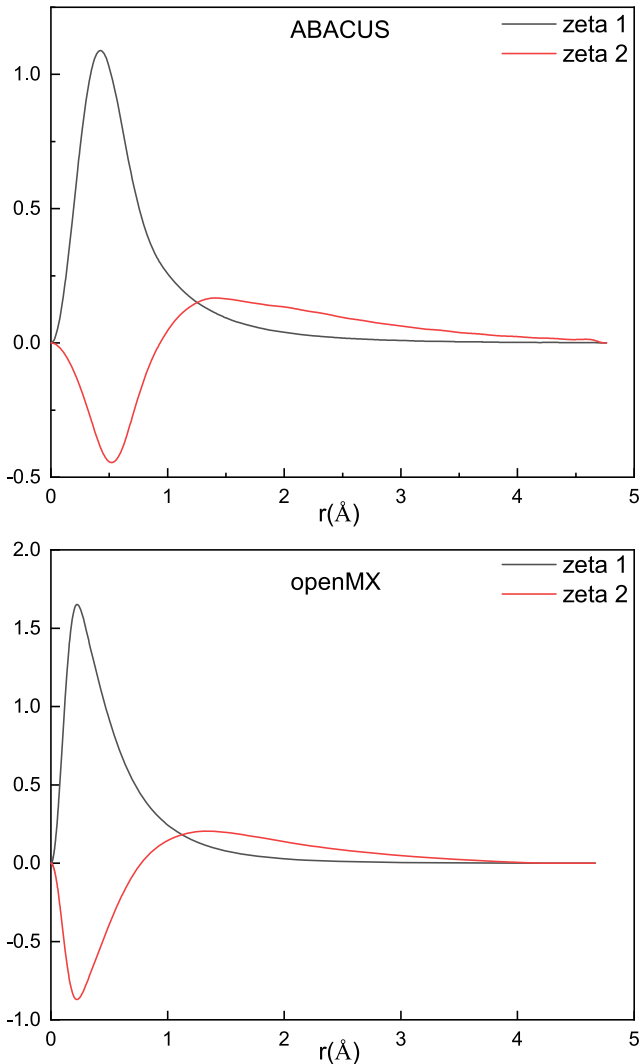


FIG. 7. Radial functions of 3d basis of Mn atom in ABACUS.

- ¹P. Hohenberg and W. Kohn, “Inhomogeneous electron gas,” *Phys. Rev.* **136**, B864–B871 (1964).
- ²W. Kohn and L. J. Sham, “Self-consistent equations including exchange and correlation effects,” *Phys. Rev.* **140**, A1133–A1138 (1965).
- ³W. Kohn, “Nobel Lecture: Electronic structure of matter—Wave functions and density functionals,” *Rev. Mod. Phys.* **71**, 1253–1266 (1999).
- ⁴A. J. Cohen, P. Mori-Sánchez, and W. Yang, “Insights into current limitations of density functional theory,” *Science* **321**, 792–794 (2008).
- ⁵C. Li, X. Zheng, N. Q. Su, and W. Yang, “Localized orbital scaling correction for systematic elimination of delocalization error in density functional approximations,” *Natl. Sci. Rev.* **5**, 203–215 (2018).
- ⁶N. Q. Su, C. Li, and W. Yang, “Describing strong correlation with fractional-spin correction in density functional theory,” *Proc. Natl. Acad. Sci. U. S. A.* **115**, 9678–9683 (2018).
- ⁷N. Q. Su, A. Mahler, and W. Yang, “Preserving symmetry and degeneracy in the localized orbital scaling correction approach,” *J. Phys. Chem. Lett.* **11**, 1528–1535 (2020).
- ⁸J. P. Perdew, R. G. Parr, M. Levy, and J. L. Balduz, “Density-functional theory for fractional particle number: Derivative discontinuities of the energy,” *Phys. Rev. Lett.* **49**, 1691–1694 (1982).
- ⁹V. Anisimov and Y. Izyumov, *Electronic Structure of Strongly Correlated Materials*, Springer Series in Solid-State Sciences Vol. 163 (Springer, Berlin, Heidelberg, 2010).
- ¹⁰B. Himmetoglu, A. Floris, S. de Gironcoli, and M. Cococcioni, “Hubbard-corrected DFT energy functionals: The LDA+ U description of correlated systems,” *Int. J. Quantum Chem.* **114**, 14–49 (2014); [arXiv:1309.3355](https://arxiv.org/abs/1309.3355).
- ¹¹J. P. Perdew and A. Zunger, “Self-interaction correction to density-functional approximations for many-electron systems,” *Phys. Rev. B* **23**, 5048 (1981).
- ¹²A. D. Becke, “Density-functional thermochemistry. III. The role of exact exchange,” *J. Chem. Phys.* **98**, 5648 (1993).
- ¹³J. Heyd, G. E. Scuseria, and M. Ernzerhof, “Hybrid functionals based on a screened Coulomb potential,” *J. Chem. Phys.* **118**, 8207 (2003).
- ¹⁴W. Metzner and D. Vollhardt, “Correlated lattice fermions in $d = \infty$ dimensions,” *Phys. Rev. Lett.* **62**, 324–327 (1989).
- ¹⁵A. Georges, G. Kotliar, W. Krauth, and M. J. Rozenberg, “Dynamical mean-field theory of strongly correlated fermion systems and the limit of infinite dimensions,” *Rev. Mod. Phys.* **68**, 13–125 (1996).
- ¹⁶V. I. Anisimov, A. I. Poteryaev, M. A. Korotin, A. O. Anokhin, and G. Kotliar, “First-principles calculations of the electronic structure and spectra of strongly correlated systems: The LDA+ U method,” *J. Phys.: Condens. Matter* **9**, 7359–7368 (1997).

- ¹⁷A. I. Lichtenstein and M. I. Katsnelson, “*Ab initio* calculations of quasiparticle band structure in correlated systems: LDA++ approach,” *Phys. Rev. B* **57**, 6884–6895 (1998).
- ¹⁸G. Kotliar, S. Y. Savrasov, K. Haule, V. S. Oudovenko, O. Parcollet, and C. A. Marianetti, “Electronic structure calculations with dynamical mean-field theory,” *Rev. Mod. Phys.* **78**, 865–951 (2006).
- ¹⁹K. Held, “Electronic structure calculations using dynamical mean field theory,” *Adv. Phys.* **56**, 829–926 (2007).
- ²⁰J. Hubbard, “Electron correlations in narrow energy bands,” *Proc. R. Soc. London, Ser. A* **276**, 238 (1963).
- ²¹M. C. Gutzwiller, “Effect of correlation on the ferromagnetism of transition metals,” *Phys. Rev. Lett.* **10**, 159 (1963).
- ²²J. Kanamori, “Electron correlation and ferromagnetism of transition metals,” *Prog. Theor. Phys.* **30**, 275 (1963).
- ²³V. I. Anisimov, J. Zaanen, and O. K. Andersen, “Band theory and Mott insulators: Hubbard U instead of Stoner I,” *Phys. Rev. B* **44**, 943–954 (1991).
- ²⁴V. I. Anisimov, I. V. Solovyev, M. A. Korotin, M. T. Czyzak, and G. A. Sawatzky, “Density-functional theory and NiO photoemission spectra,” *Phys. Rev. B* **48**, 16929–16934 (1993).
- ²⁵A. B. Shick, A. I. Liechtenstein, and W. E. Pickett, “Implementation of the LDA+U method using the full-potential linearized augmented plane-wave basis,” *Phys. Rev. B* **60**, 10763–10769 (1999).
- ²⁶See <https://elk.sourceforge.io/> for information about the Elk software.
- ²⁷O. Bengone, M. Alouani, P. Blöchl, and J. Hugel, “Implementation of the projector augmented-wave LDA+U method: Application to the electronic structure of NiO,” *Phys. Rev. B* **62**, 16392–16401 (2000).
- ²⁸B. Amadon, F. Jollet, and M. Torrent, “ γ and β cerium: LDA+U calculations of ground-state parameters,” *Phys. Rev. B* **77**, 155104 (2008).
- ²⁹P. Giannozzi, S. Baroni, N. Bonini, M. Calandra *et al.*, “QUANTUM ESPRESSO: A modular and open-source software project for quantum simulations of materials,” *J. Phys.: Condens. Matter* **21**, 395502 (2009).
- ³⁰M. Cococcioni and S. de Gironcoli, “Linear response approach to the calculation of the effective interaction parameters in the LDA+U method,” *Phys. Rev. B* **71**, 035105 (2005).
- ³¹B. Delley, “From molecules to solids with the DMol³ approach,” *J. Chem. Phys.* **113**, 7756–7764 (2000).
- ³²K. Koepernik and H. Eschrig, “Full-potential nonorthogonal local-orbital minimum-basis band-structure scheme,” *Phys. Rev. B* **59**, 1743–1757 (1999).
- ³³J. M. Soler, E. Artacho, J. D. Gale, A. García, J. Junquera, P. Ordejón, and D. Sánchez-Portal, “The SIESTA method for *ab initio* order-N materials simulation,” *J. Phys.: Condens. Matter* **14**, 2745–2779 (2002).
- ³⁴T. Ozaki, H. Kino, J. Yu, M. Han, N. Kobayashi, M. Ohfuti, F. Ishii, and T. Ohwaki, User’s manual of OpenMX, <http://www.openmx-square.org>, 2008.
- ³⁵V. Blum, R. Gehrke, F. Hanke, P. Havu, V. Havu, X. Ren, K. Reuter, and M. Scheffler, “*Ab initio* molecular simulations with numeric atom-centered orbitals,” *Comput. Phys. Commun.* **180**, 2175 (2009).
- ³⁶P. Li, X. Liu, M. Chen, P. Lin, X. Ren, L. Lin, C. Yang, and L. He, “Large-scale *ab initio* simulations based on systematically improvable atomic basis,” *Comput. Mater. Sci.* **112**, 503–517 (2016).
- ³⁷X. Ren, P. Rinke, V. Blum, J. Wieferink, A. Tkatchenko, A. Sanfilippo, K. Reuter, and M. Scheffler, “Resolution-of-identity approach to Hartree–Fock, hybrid density functionals, RPA, MP2 and GW with numeric atom-centered orbital basis functions,” *New J. Phys.* **14**, 053020 (2012).
- ³⁸S. V. Levchenko, X. Ren, J. Wieferink, R. Johann, P. Rinke, V. Blum, and M. Scheffler, “Hybrid functionals for large periodic systems in an all-electron, numeric atom-centered basis framework,” *Comput. Phys. Commun.* **192**, 60 (2015).
- ³⁹P. Lin, X. Ren, and L. He, “Accuracy of localized resolution of the identity in periodic hybrid functional calculations with numerical atomic orbitals,” *J. Phys. Chem. Lett.* **11**, 3082 (2020).
- ⁴⁰P. Lin, X. Ren, and L. He, “Efficient hybrid density functional calculations for large periodic systems using numerical atomic orbitals,” *J. Chem. Theory Comput.* **17**, 222 (2021).
- ⁴¹M. N. Tahir and X. Ren, “Comparing particle-particle and particle-hole channels of the random phase approximation,” *Phys. Rev. B* **99**, 195149 (2019).
- ⁴²X. Ren, F. Merz, H. Jiang, Y. Yao, M. Rampp, H. Lederer, V. Blum, and M. Scheffler, “All-electron periodic G_0W_0 implementation with numerical atomic orbital basis functions: Algorithm and benchmarks,” *Phys. Rev. Mater.* **5**, 013807 (2021).
- ⁴³See <https://siesta-project.org/siesta/> for information about the SIESTA software.
- ⁴⁴M. J. Han, T. Ozaki, and J. Yu, “ $O(N)$ LDA+U electronic structure calculation method based on the nonorthogonal pseudoatomic orbital basis,” *Phys. Rev. B* **73**, 045110 (2006).
- ⁴⁵M. Kick, K. Reuter, and H. Oberhofer, “Intricacies of DFT+U, not only in a numeric atom centered orbital framework,” *J. Chem. Theory Comput.* **15**, 1705 (2019).
- ⁴⁶R. M. Martin, *Electronic Structure* (Cambridge University Press, 2004).
- ⁴⁷A. I. Liechtenstein, V. I. Anisimov, and J. Zaanen, “Density-functional theory and strong interactions: Orbital ordering in Mott-Hubbard insulators,” *Phys. Rev. B* **52**, R5467–R5470 (1995).
- ⁴⁸P. H. Dederichs, S. Blügel, R. Zeller, and H. Akai, “Ground states of constrained systems: Application to cerium impurities,” *Phys. Rev. Lett.* **53**, 2512–2515 (1984).
- ⁴⁹M. R. Norman and A. J. Freeman, “Model supercell local-density calculations of the 3d excitation spectra in NiO,” *Phys. Rev. B* **33**, 8896–8898 (1986).
- ⁵⁰O. Gunnarsson, O. K. Andersen, O. Jepsen, and J. Zaanen, “Density-functional calculation of the parameters in the Anderson model: Application to Mn in CdTe,” *Phys. Rev. B* **39**, 1708–1722 (1989).
- ⁵¹F. Aryasetiawan, M. Imada, A. Georges, G. Kotliar, S. Biermann, and A. I. Liechtenstein, “Frequency-dependent local interactions and low-energy effective models from electronic structure calculations,” *Phys. Rev. B* **70**, 195104 (2004).
- ⁵²T. Miyake and F. Aryasetiawan, “Screened Coulomb interaction in the maximally localized Wannier basis,” *Phys. Rev. B* **77**, 085122 (2008).
- ⁵³T. Miyake, F. Aryasetiawan, and M. Imada, “*Ab initio* procedure for constructing effective models of correlated materials with entangled band structure,” *Phys. Rev. B* **80**, 155134 (2009).
- ⁵⁴R. Sakuma and F. Aryasetiawan, “First-principles calculations of dynamical screened interactions for the transition metal oxides MO (M=Mn, Fe, Co, Ni),” *Phys. Rev. B* **87**, 165118 (2013).
- ⁵⁵E. R. Ylvisaker, W. E. Pickett, and K. Koepernik, “Anisotropy and magnetism in the LSDA+U method,” *Phys. Rev. B* **79**, 035103 (2009).
- ⁵⁶S. L. Dudarev, G. A. Botton, S. Y. Savrasov, C. J. Humphreys, and A. P. Sutton, “Electron-energy-loss spectra and the structural stability of nickel oxide: An LSDA+U study,” *Phys. Rev. B* **57**, 1505–1509 (1998).
- ⁵⁷F. Bultmark, F. Cricchio, O. Gränäs, and L. Nordström, “Multipole decomposition of LDA+U energy and its application to actinide compounds,” *Phys. Rev. B* **80**, 035121 (2009).
- ⁵⁸M. R. Norman, “Calculation of effective Coulomb interaction for Pr³⁺, U⁴⁺, and UPt₃,” *Phys. Rev. B* **52**, 1421–1424 (1995).
- ⁵⁹Y. C. Wang and H. Jiang, “Local screened Coulomb correction approach to strongly correlated d-electron systems,” *J. Chem. Phys.* **150**, 154116 (2019).
- ⁶⁰D. R. Hamann, “Optimized norm-conserving Vanderbilt pseudopotentials,” *Phys. Rev. B* **88**, 085117 (2013).
- ⁶¹M. Schlipf and F. Gygi, “Optimization algorithm for the generation of ONCV pseudopotentials,” *Comput. Phys. Commun.* **196**, 36–44 (2015).
- ⁶²P. Scherpelz, M. Govoni, I. Hamada, and G. Galli, “Implementation and validation of fully relativistic GW calculations: Spin-orbit coupling in molecules, nanocrystals, and solids,” *J. Chem. Theory Comput.* **12**, 3523–3544 (2016).
- ⁶³M. Chen, G.-C. Guo, and L. He, “Systematically improvable optimized atomic basis sets for *ab initio* calculations,” *J. Phys.: Condens. Matter* **22**, 445501 (2010).
- ⁶⁴W. Setyawan and S. Curtarolo, “High-throughput electronic band structure calculations: Challenges and tools,” *Comput. Mater. Sci.* **49**, 299–312 (2010).
- ⁶⁵S. K. Panda, S. Bhowal, A. Delin, O. Eriksson, and I. Dasgupta, “Effect of spin orbit coupling and Hubbard U on the electronic structure of IrO₂,” *Phys. Rev. B* **89**, 155102 (2014).
- ⁶⁶J. P. Perdew, K. Burke, and M. Ernzerhof, “Generalized gradient approximation made simple,” *Phys. Rev. Lett.* **77**, 3865–3868 (1996).

- ⁶⁷T. Ozaki, "Variationally optimized atomic orbitals for large-scale electronic structures," *Phys. Rev. B* **67**, 155108 (2003).
- ⁶⁸T. Ozaki and H. Kino, "Numerical atomic basis orbitals from H to Kr," *Phys. Rev. B* **69**, 195113 (2004).
- ⁶⁹F. Tran, P. Blaha, K. Schwarz, and P. Novák, "Hybrid exchange-correlation energy functionals for strongly correlated electrons: Applications to transition-metal monoxides," *Phys. Rev. B* **74**, 155108 (2006).
- ⁷⁰Y.-C. Wang, Z.-H. Chen, and H. Jiang, "The local projection in the density functional theory plus *U* approach: A critical assessment," *J. Chem. Phys.* **144**, 144106 (2016).
- ⁷¹L. Messick, W. C. Walker, and R. Glosser, "Direct and temperature-modulated reflectance spectra of MnO, CoO, and NiO," *Phys. Rev. B* **6**, 3941–3949 (1972).
- ⁷²H. K. Bowen, D. Adler, and B. H. Auker, "Electrical and optical properties of FeO," *J. Solid State Chem.* **12**, 355–359 (1975).
- ⁷³R. J. Powell and W. E. Spicer, "Optical properties of NiO and CoO," *Phys. Rev. B* **2**, 2182–2193 (1970).
- ⁷⁴G. A. Sawatzky and J. W. Allen, "Magnitude and origin of the band gap in NiO," *Phys. Rev. Lett.* **53**, 2339–2342 (1984).
- ⁷⁵S. Hüfner, J. Osterwalder, T. Riesterer, and F. Hulliger, "Photoemission and inverse photoemission spectroscopy of NiO," *Solid State Commun.* **52**, 793–796 (1984).
- ⁷⁶A. K. Cheetham and D. A. O. Hope, "Magnetic ordering and exchange effects in the antiferromagnetic solid solutions $Mn_xNi_{1-x}O$," *Phys. Rev. B* **27**, 6964–6967 (1983).
- ⁷⁷B. E. F. Fender, A. J. Jacobson, and F. A. Wedgwood, "Covalency parameters in MnO, α -MnS, and NiO," *J. Chem. Phys.* **48**, 990–994 (1968).
- ⁷⁸W. L. Roth, "Magnetic structures of MnO, FeO, CoO, and NiO," *Phys. Rev.* **110**, 1333–1341 (1958).
- ⁷⁹D. C. Khan and R. A. Erickson, "Magnetic form factor of Co^{++} ion in cobaltous oxide," *Phys. Rev. B* **1**, 2243–2249 (1970).
- ⁸⁰H. Jiang, R. I. Gomez-Abal, P. Rinke, and M. Scheffler, "First-principles modeling of localized d states with the GW@LDA+U approach," *Phys. Rev. B* **82**, 045108 (2010).
- ⁸¹G. Pepy, "Spin waves in MnO; from 4°K to temperatures close to T_N ," *J. Phys. Chem. Solids* **35**, 433–444 (1974).
- ⁸²R. Shanker and R. A. Singh, "Analysis of the exchange parameters and magnetic properties of NiO," *Phys. Rev. B* **7**, 5000–5005 (1973).
- ⁸³X. Feng and N. M. Harrison, "Magnetic coupling constants from a hybrid density functional with 35% Hartree-Fock exchange," *Phys. Rev. B* **70**, 092402 (2004).
- ⁸⁴See <http://abacus.ustc.edu.cn> for the ABACUS software.